

1

Revision 1

2

Ferruginous seawater facilitates the transformation of glauconite to chamosite: an example from the Mesoproterozoic Xiamaling Formation of North China

4

5 **DONGJIE TANG^{1,2}, XIAOYING SHI^{*1,3}, GANQING JIANG⁴, XIQIANG ZHOU⁵,**
6 **QING SHI^{1,2}**

7

8 ¹State Key Laboratory of Biogeology and Environmental Geology, China University of
9 Geosciences, Beijing 100083, China

10 ²Institute of Earth Sciences, China University of Geosciences, Beijing 100083, China

11 ³School of Earth Sciences and Resources, China University of Geosciences, Beijing
12 100083, China

13 ⁴Department of Geoscience, University of Nevada, Las Vegas, NV 89154-4010, USA

14 ⁵Key Lab of Petroleum Resources Research, Institute of Geology and Geophysics,
15 Chinese Academy of Sciences, Beijing 100029, China

16 *Corresponding author. E-mail: dongjtang@126.com (D. Tang), shixyb@cugb.edu.cn (X.
17 Shi); Tel.: +86 10 82321737; fax: +86 10 82321737.

18

19

ABSTRACT

20 Berthierine and chamosite are iron-rich clay minerals that have similar chemical
21 compositions. Berthierine forms at low temperature (25–45°C) during early diagenesis
22 and may transfer to chamosite at temperatures of $\geq 70^\circ\text{C}$. Because the formation of
23 berthierine and chamosite requires significant amount of Fe^{2+} supply, their presence in

24 marine sediments is often used as a mineral proxy for ferruginous conditions in porewater.
25 Recent studies reveal that the Precambrian oceans were characterized by pervasive
26 ferruginous water-column conditions that may favor the formation of iron-rich clay
27 minerals like berthierine and chamosite. To evaluate if ferruginous water-column
28 conditions in the Precambrian ocean played a role on iron-rich clay mineral formation,
29 we conducted an integrated petrographic, mineralogical, and geochemical study on the
30 chamosite- and glauconite-bearing strata of the Mesoproterozoic Xiamaling Formation
31 (~1.40–1.35 Ga) in North China. Petrographic, XRD, SEM and EDS analyses show that
32 the chamosites of the Xiamaling Formation was transferred from glauconite, with
33 berthierine as an intermediate mineral phase during early diagenesis. Geochemical
34 analyses indicate that a complete transformation from glauconite-dominated to
35 chamosite-dominated end-members (samples) requires an addition of a large amount of
36 Fe (16.9 wt%), Mg (2.4 wt%), and a small amount of Al (1.4 wt%), but a simultaneous
37 release of Si (11.8 wt%) and K (6.0 wt%). Considering that the glauconite- and
38 chamosite-bearing strata are devoid of iron-rich detrital minerals (e.g., biotite and iron
39 oxides) and lack evidence of hydrothermal alteration, the required Fe^{2+} for
40 glauconite-berthierine-chamosite transformation was most likely from Fe^{2+} -rich
41 (ferruginous) seawater, which may have promoted glauconite-berthierine transformation
42 at the very early diagenetic stage when Fe^{2+} exchange between porewater and seawater
43 was still available. This interpretation is consistent with the high $\text{Fe}_{\text{HR}}/\text{Fe}_{\text{T}}$ (but low
44 $\text{Fe}_{\text{py}}/\text{Fe}_{\text{HR}}$), Fe/Al , and V/Al ratios from the hosting strata that support ferruginous
45 depositional environments. Because most Precambrian strata have passed the oil window
46 temperature ($>50^{\circ}\text{C}$), the preservation of berthierine would be rare and chamosite should

47 be the representative iron-rich clay mineral. Thus, the abundance of chamosite in
48 fine-grained, marine siliciclastic sediments may be used as a mineral indicator of
49 ferruginous water-column conditions.

50 **Keywords:** Glauconite; Berthierine; Chamosite; Seawater redox conditions;
51 Mesoproterozoic; Xiamaling Formation

52

53

INTRODUCTION

54 Chamosite $[(\text{Fe}^{2+}, \text{Mg}, \text{Al}, \text{Fe}^{3+})_6(\text{Si}_{4-x}, \text{Al}_x)\text{O}_{10}(\text{OH})_8]$ is an Fe-rich chlorite with 2:1+1
55 trioctahedral structures, and its presence in sedimentary rocks is commonly regarded as
56 the result of berthierine transformation at temperature $\geq 70^\circ\text{C}$ during diagenesis (Young
57 and Taylor 1989; Velde 1995; Hornibrook and Longstaffe 1996; Kozłowska and
58 Maliszewska 2015). Berthierine $[(\text{Fe}^{2+}, \text{Mg}, \text{Al})_{2-3}(\text{Si}, \text{Al})_2\text{O}_5(\text{OH})_4]$, a dark green to brown
59 mineral (Hornibrook and Longstaffe 1996), shares similar chemical composition with
60 chamosite, but has a trioctahedral 1:1 layered silicate structure that has a basal spacing of
61 0.7 nm (serpentine group) (Bhattacharyya 1983; Rivas-Sanchez et al. 2006). Berthierine
62 is commonly considered to be characteristic of marine deposits (Taylor and Curtis 1995;
63 Ryan and Hillier 2002; Taylor et al. 2002), although it was also reported from
64 brackish-water deposits (Taylor 1990), coal beds (Iijima and Matsumoto 1982; Dai and
65 Chou 2007; Zhao et al. 2016), laterites (Fritz and Toth 1997), and some hydrothermal
66 deposits (Rivas-Sanchez et al. 2006).

67 Berthierine in marine sediments and sedimentary rocks is commonly thought to be
68 formed through diagenetic recrystallization of glauconite, odinite, kaolinite and iron
69 oxide-hydroxide, or other similar precursor minerals (Odin et al. 1988; Drits et al. 2001;

70 [Rivard et al. 2013](#); [Fu et al. 2015](#); [Kozłowska and Maliszewska 2015](#); [Mu et al. 2015](#)).
71 Formation of berthierine requires warm seawater ([Hornibrook and Longstaffe 1996](#)) and
72 reducing diagenetic conditions with limited sulfate reduction (i.e., ferruginous but not
73 euxinic), because the crystallization of berthierine requires the incorporation of reduced
74 iron (Fe^{2+}) ([Bhattacharyya 1983](#); [Taylor 1990](#); [Velde 1995](#); [Fritz and Toth 1997](#); [Sheldon](#)
75 [and Retallack 2002](#); [Worden and Morad 2003](#); [Rivard et al. 2013](#)). Chamosite, which has
76 a Fe-rich berthierine precursor, would require similar chemical conditions to form, in
77 addition to higher temperature requirement ($\geq 70^\circ\text{C}$) through burial or hydrothermal
78 processes.

79 Previous studies mainly focused on the source of iron and pore-water redox
80 conditions required for the formation of berthierine and chamosite (e.g., [Odin et al. 1988](#);
81 [Velde 1995](#); [Sheldon and Retallack 2002](#); [Kozłowska and Maliszewska 2015](#)). In most
82 cases, iron-rich porewater (derived from iron-bearing freshwater) seems to be the
83 required condition for berthierine precipitation during early diagenesis. However, the
84 potential impacts of seawater chemistry on the formation of berthierine have not been
85 adequately dealt with. This is particularly important for the berthierine and chamosite in
86 stratigraphic successions of Precambrian ages, during which ferruginous seawater
87 conditions may have prevailed even in shallow-water environments (e.g., [Canfield et al.](#)
88 [2008](#); [Planavsky et al. 2011](#); [Poulton and Canfield 2011](#); [Tang et al. 2016](#)).

89 In this paper we report a comprehensive study of the chamosite and glauconite from
90 the Mesoproterozoic Xiamaling Formation (1.40–1.35 Ga) of the North China Platform
91 ([Figs. 1 and 2](#)), using integrated data obtained from field observations, petrography, XRD,
92 SEM, quantitative EDS, XRF and ICP-MS analyses. Mineralogical, geochemical, and

93 textural results confirm that chamosite (and its precursor mineral, berthierine) is
94 transformed from iron-poor glauconite $[(K,Na)(Fe,Al,Mg)_2(Si,Al)_4O_{10}(OH)_2]$. In
95 combination with geochemical data from the hosting rocks, we demonstrate that Fe^{2+}
96 supply from ferruginous seawater is critical for the formation of berthierine and
97 chamosite (in later stage). We propose that the presence of Fe-rich clay minerals such as
98 berthierine and chamosite in Precambrian stratigraphic successions may be used as an
99 indicator for ferruginous seawater conditions.

100

101

GEOLOGICAL SETTING

102 Regional stratigraphy and age constraints

103 In association with the breaking-up of supercontinent Columbia ([Zhao et al. 2003,](#)
104 [2004, 2011;](#) [Zhang et al. 2009, 2012, 2017](#)) to the assembly of Rodinia ([Li et al. 2008](#)),
105 the North China Platform accumulated a thick (~9000 m) sedimentary succession during
106 the Proterozoic. This succession is subdivided into three groups ([Fig. 2](#)), i.e., the
107 Changcheng Group (1660–1600 Ma, Pt₁), Jixian Group (1600–1400 Ma, Pt₂), and the
108 Qingbaikou Group (1000–800 Ma, Pt₃), with a significant hiatus of ~400 Ma between the
109 Jixian and Qingbaikou groups ([Gao et al. 2009](#)). The deposition of the Chuanlinggou
110 ironstone (~1.64 Ga) in the low part of the Changcheng Group marks a major change in
111 depositional environment and tectonic setting of the North China Platform in response to
112 the initial breakup of supercontinent Columbia ([Tang et al. 2015](#)). The widespread ~1.35
113 Ga diabase sills and ~1.33 Ga bimodal magmatic rocks, shortly after the deposition of the
114 Xiamaling Formation (~1.40–1.35 Ga), may record the final separation of the North
115 China Craton (NCC) from supercontinent Columbia ([Zhang et al. 2009, 2011, 2015,](#)

116 2017). A significant uplift after the Qingbaikou Group, which is thought to have resulted
117 from the formation of supercontinent Rodinia (Wang et al. 2000; Lu et al. 2008), exposed
118 the Proterozoic basement of the NCC until mid Cambrian (Zhou et al. 2006).

119 Paleomagnetic study suggests that during the deposition of the Xiamaling Formation,
120 the uppermost part of the Jixian Group, the North China Platform lay between 10°N and
121 30°N (Evans and Mitchell 2011; Zhang et al. 2012). Many studies suggested that the
122 Xiamaling Formation was deposited in an extensional setting (Zhang et al. 2009, 2012,
123 2017), though a back-arc setting was also suggested (Meng et al. 2011) based on a study
124 of volcanic ash beds in the formation.

125 In recent years, a number of zircon U–Pb ages (including ICP–MS, SHRIMP and
126 TIMS methods) have been obtained from the Proterozoic succession of North China (Lu
127 and Li 1991; Gao et al. 2007, 2008a, 2008b; Lu et al. 2008; Su et al. 2008, 2010, 2014; Li
128 et al. 2010, 2013, 2014; Zhang et al. 2013, 2015; Duan et al. 2014), providing
129 geochronologic constraints for the stratigraphic subdivisions (Fig. 2). Based on the
130 high-precision zircon ages of 1384.4±1.4 Ma and 1392.2±1.0 Ma from the lower part
131 (Zhang et al. 2015) and the zircon and baddeleyite ages of 1345±12 Ma and 1353±14 Ma
132 from the diabase sills in the upper part (Zhang et al. 2009; Li et al. 2013; Su 2016), the
133 duration of the Xiamaling Formation is well constrained between ~1.40 Ga and ~1.35 Ga.

134

135 **Sedimentary facies and depositional environments**

136 The Xiamaling Formation lies disconformably between the underlying Tieling
137 Formation and the overlying Changlongshan Formation (Fig. 1). From the base to the top,
138 the Xiamaling Formation forms a large transgressive-regressive cycle, predominated by

139 dark siltstone and shale that are subdivided into four members (Fig. 1). Member-I is
140 predominated by gray to greenish silty shales, with some siltstone interbeds (Fig. 3a) and
141 many siderite concretions (Fig. 3b). The lowermost part of this member is characterized
142 by purplish gravely sandstone (Fig. 3c), particularly in the Zhaojiashan section, Hebei
143 Province, which may represent lag deposits along a transgressive surface above an
144 unconformity at the top of stromatolite-rich dolostones of the Tieling Formation.
145 Member-II consists of four lithologically distinct intervals (Fig. 1): the lower part is
146 characterized by greenish glauconite- and chamosite-rich, argillaceous siltstone, silty
147 shale, and fine-grained sandstone; the lower middle part consists of interbedded green
148 and purplish shales with ankerite-rich carbonate lenticles; the upper middle part is
149 predominated by greenish, glauconite-rich shale; and the upper part comprise mainly gray
150 to black, organic-rich shale with some carbonate concretions (Figs. 3d–g). Member-III is
151 composed predominantly of black shale and partially silicified black shale (Fig. 3h), with
152 some silty mudstone interbeds and a marly dolostone layer at the base. The lower part of
153 Member-IV consists of alternating black and greenish shale, with some marly dolostone
154 interbeds. The upper part of Member IV consists of a regressive sequence from shale to
155 yellowish siltstone, which is unconformably overlain by medium-grained quartz
156 sandstone of the Changlongshan Formation.

157 The silty shale and argillaceous fine-grained sandstone in Member-I and -II show
158 well-preserved horizontal laminations but wave-agitated structures or cross-beddings are
159 absent, suggesting deposition from subtidal environments below fair-weather wave base.
160 Black shales of Member-III and lower Member-IV were likely deposited in deep subtidal
161 environments below storm wave base (>60 m) (Meng et al. 2011; Zhang et al. 2015,

162 2016). Organic matter preserved in the Xiamaling Formation is ranked as immature to
163 early thermal mature, with burial temperatures of $\leq 90^{\circ}\text{C}$ (Zhang et al. 2015).

164

165 MATERIALS AND METHODS

166 Samples analyzed in this study are from Member-I and -II of the Xiamaling
167 Formation and were collected from a freshly exposed road cut at the Zhaojiashan section
168 (N: $40^{\circ}28'27.40''$, E: $115^{\circ}23'30.78''$), Hebei Province (Fig. 1). Collected samples were cut
169 into chips and only the fresh, central parts of the samples are used for thin section and
170 mineralogical/geochemical analyses. For the latter purpose, fresh sample chips were
171 cleaned, dried, and grounded into powders (~200 mesh) in agate mortar to avoid any
172 metal contact. Samples with well-preserved glauconite and chamosite were selected for
173 microscope and SEM observations, and for mineral (XRD) and chemical (EDS and trace
174 element) analyses. Macroscopic features were observed in the field and on polished slabs.
175 Microfabrics were observed on thin sections with a Stereo Discovery V20 microscope for
176 large scope and a Zeiss Axio Scope A1 microscope for high magnification.
177 Ultrastructures were studied using a Zeiss Supra 55 field emission scanning electron
178 microscope (FESEM) under 20 kV accelerating voltage with a working distance of 15
179 mm, at the State Key Laboratory of Biology and Environmental Geology, China
180 University of Geosciences (Beijing). Secondary electron imaging detector (SE2) was
181 used to characterize topographic features, and an AsB detector was used to characterize
182 compositional difference (backscattered electron, BSE, image). Samples were coated
183 with ~10-nm-thick platinum for electric conduction before analysis.

184 Quantitative element concentrations of micron-sized spots were analyzed by an

185 Oxford energy dispersive X-ray spectrometer (EDS) connected to the FESEM, operated
186 at 20 kV with a working distance of 15 mm, specimen current of 200 nA, and beam
187 diameter of $\sim 1 \mu\text{m}$, at the State Key Laboratory of Biogeology and Environmental
188 Geology, China University of Geosciences (Beijing). Minerals as well as synthetic phases
189 (MINM25-53) were used as standards. Duplicate analyses of individual points showed
190 analytical error less than 1%.

191 Trace metals and major elements were measured with a handheld energy dispersive
192 XRF spectrometer (HHXRF) model Xsort with Rh anode from Spectro. The X-ray
193 absorption was identified with the Spectro software where fundamental parameters were
194 used to convert counts to concentrations by calibration to a standardized metal alloy coin
195 with known trace element composition (supplied by manufacturer). Powdered rock
196 samples in vials were covered with 4- μm -thick polypropylene X-ray film and measured
197 upside down in the XRF stand. Powder thickness was generally $>5 \text{ mm}$ to achieve
198 optimal noise normalization. The counts were made for 120s on 10-KHz beam and 60s
199 on 40-KHz beam, for a total of 3 min. A certified reference material (GBW07107) was
200 measured after every five samples, and the relative SD for all of the analyzed major
201 elements was generally $<8\%$, and the relative SD for V was $<10\%$.

202 Three bulk rock samples (random power) and 26 purified clay mineral samples
203 (oriented power) were chosen for XRD analysis. Purified clay mineral samples were
204 separated from 200-mesh powders of bulk rock through sedimentation and centrifuge.
205 Oriented powder aggregates were made by concentrating 50–100 mg of clay in distilled
206 water and letting the clay slurry drop onto glass slides ($2.7 \times 4.6 \text{ cm}$). The samples were
207 scanned after air-drying and ethylene glycol-solvated. The powder slides were scanned

208 from 4° to 70° with a step size of 0.02° 2θ and a scan speed of 1°/min, using nickel filter
209 copper radiation in an SmartLab X-Ray Diffractometer at China University of
210 Geosciences (Beijing).

211 Interstratification of 7 Å (berthierine) layers and 14 Å (chamosite) layers can be
212 difficult to detect because $d_{001}\text{Chamosite (Ch)} \approx 2d_{001}\text{Berthierine (Ber)}$, and Ber peaks
213 essentially overlap with even-order Ch peaks. However, random interstratification of Ber
214 and Ch causes broadening of the odd-order Ch peaks proportional to the amount of 7 Å
215 material, making Ber-Ch interstratification identifiable and quantifiable (Reynolds et al.
216 1992; Ryan and Reynolds Jr 1996). The percentage of Ber can be determined by the
217 equation:

$$218 \quad \% \text{Ber} = -0.51 + 24 * (\beta(005)^{1.25} - \beta(004)^{1.25})^{(1/1.25)},$$

219 where $\beta(004)$ and $\beta(005)$ are the peak widths at one-half height (in degrees 2Theta) for
220 the Ch 004 and 005 peaks, respectively. The results are within ~95% accuracy of the
221 reported value (Ryan and Reynolds Jr 1996).

222 To determine polytypism of Ber-Ch, random powder mounts were prepared by
223 freeze-drying solutions of approximately 1 g of powder in 50–100 mL of distilled water
224 (Ryan and Reynolds Jr 1996). Ber-Ch polytypes were identified by comparison with
225 published patterns (Ryan and Reynolds Jr 1996). The *Ibb* polytype has its (204) and (206)
226 peaks at ~42° and ~51° 2Theta, respectively, while the *Iaa* polytype has its (204) and
227 (206) peaks at ~45° and ~55° 2Theta, respectively (Ryan and Reynolds Jr 1996).

228 Three representative samples were selected for TEM observation to identify Ber-Ch
229 interstratification. Samples for TEM analyses were separated from 200-mesh sample
230 powders through sedimentation and centrifuge. The collected clay powders were placed

231 in an agate bowl which has been ultrasonically cleaned in deionized water. Anhydrous
232 ethanol was added to the agate bowl and milled for 5 minutes. The sample was dropped
233 into a copper mesh before the ethanol was completely volatilized and was dried under an
234 infrared lamp for 4 hours. The sample on the copper mesh was analyzed using a Hitachi
235 H-8100 TEM, equipped with a tungsten filament electron source (operated at 200 kV),
236 and an EDAX X-ray analyzer with an ultrathin window.

237 The redox conditions of the depositional environments are determined by the Fe
238 speciation. The highly reactive Fe (Fe_{HR}) is broadly apportioned into four different pools
239 ($Fe_{HR} = Fe_{carb} + Fe_{ox} + Fe_{mag} + Fe_{py}$): carbonate Fe (Fe_{carb}), oxide Fe (Fe_{ox}), magnetite Fe
240 (Fe_{mag}) and pyrite Fe (Fe_{py}) (Poulton and Canfield 2005; Poulton and Canfield 2011).
241 Fe_{carb} was extracted from iron carbonate minerals with sodium acetate solution adjusted
242 to pH=4.5 by addition of trace-metal grade acetic acid; Fe_{ox} was extracted from iron
243 oxide/oxyhydroxide phase using a 50 g/L sodium dithionite solution buffered to pH=4.8
244 with 0.2 M sodium citrate and trace-metal grade acetic acid; Fe_{mag} was extracted from
245 magnetite by a 0.2 M ammonium oxalate and 0.17 M oxalic acid solution. All extracts
246 were diluted and then analyzed by atomic absorption spectroscopy for their Fe contents at
247 the Institute of Geology and Geophysics, Chinese Academy of Sciences. Fe_{py} was
248 calculated by stoichiometry from Cr-reduction of pyrite (Canfield et al. 1986). Fe_T was
249 analyzed by automatic X-ray fluorescence spectrometer (XRF-1800) on fused glass disks
250 at the China University of Geosciences (Beijing).

251

252

RESULTS

253 **Features of glauconite and chamosite**

254 **Occurrence of glauconite and chamosite.** Glauconite and chamosite are rich in
255 silty shale, siltstone and argillaceous fine-grained sandstone of Member-I and -II of the
256 Xiamaling Formation (Fig. 1). Microscopic observation confirms that these two members
257 are dominated by silty shale and argillaceous fine-grained sandstone without
258 wave-agitated structures, but some horizontal microbial mat laminations can be observed
259 (Fig. 4a). Glauconite is green in color and occurs in two distinct forms: (1) autochthonous
260 (Figs. 4b and 4c), and (2) allochthonous (Fig. 4d). Autochthonous glauconite appears as
261 pore cement with irregular outlines, occasionally trapping quartz particles (Fig. 4b).
262 Allochthonous glauconite particles have subrounded–subangular shapes (Fig. 4d) that are
263 morphologically similar to detrital quartz particles. They are probably originated from
264 autochthonous glauconite through short distance transportation. Compactional distortion
265 of some allochthonous glauconite particles can be observed (Fig. 4d). BSE and element
266 mapping show that both autochthonous and allochthonous glauconites have been partially
267 transformed to chamosite. In some chamosite-rich samples, the outline of parent
268 glauconite particles can still be identified, indicating the transformation from glauconite
269 to chamosite (Fig. 4e). Chamosite is yellowish brown in color, and is mainly formed
270 through *in situ* transformation from glauconite particles (Fig. 4e).

271 **Substrates of glauconite and chamosite.** In both glauconite- and chamosite-rich
272 samples, quartz particles are the predominant substrate (Figs. 4f–h). Pyrite, rutile and
273 albite are minor; terrigenous iron-rich minerals, such as biotite, are absent (further
274 supported by XRD results). Quartz particles are subrounded to subangular in shape and
275 can be further divided into phaneritic quartz and aphanitic chert particles; the latter is the
276 predominant form (Figs. 4f–h).

277 **Mineralogy of glauconite and chamosite.** Three bulk rock samples (random power;
278 [Fig. 5a](#)) and twenty-six purified clay mineral samples (oriented power; [Figs. 5b–d](#)) were
279 analyzed. On the XRD pattern, berthierine is a mineral characterized by an intense
280 reflection (001) at 0.705 nm, and two reflections (020) and (002) of lesser intensity at
281 0.466 nm and 0.352 nm, respectively. In contrast, high-iron chlorites (e.g. chamosite) are
282 characterized by the presence of strong reflections of (002) and (004) at 0.709 and 0.353
283 nm, respectively, and relatively weak reflections of (001), (003) and (005) at 1.425, 0.473
284 and 0.284 nm, respectively ([Kozłowska and Maliszewska 2015](#)). The air-dried bulk rock
285 samples exhibit strong reflections at 0.709 nm and 0.354 nm, and relatively weak
286 reflections at 1.429, 0.474 and 0.284 nm, confirming the presence of chamosite, while the
287 weak reflection at 0.466 nm probably indicates the occurrence of minor berthierine
288 ([Kozłowska and Maliszewska 2015](#)). The intense basal reflection (001) at 1.014 nm
289 *d*-spacing and weak basal reflections (003) at 0.33 nm, (004) at 0.25 nm, (005) at 0.20 nm,
290 (11 $\bar{2}$) at 0.366 nm and (112) at 0.308 nm *d*-spacing are the characteristic peaks of
291 glauconite ([Fig. 5](#)). The weak basal reflections (040) at 0.32 nm, ($\bar{3}$ $\bar{1}$ 1) at 0.27 nm,
292 (5 $\bar{1}$ $\bar{3}$) at 0.16 nm *d*-spacing are the characteristic peaks of anorthose (~5%, [Fig. 5a](#)),
293 and the weak reflection (020) at 0.447 nm is the characteristic peak of kaolinite ([Fig. 5](#)).
294 The three air-dried bulk rock samples exhibit intense quartz peaks (~60 wt%) but weak
295 glauconite (about 5–15 wt%), chamosite (about 10–25 wt%) and berthierine peaks in the
296 XRD spectrum ([Fig. 5a](#)). Signals of glauconite and chamosite in the three samples are
297 variable, suggesting varied chamosite and glauconite contents ([Fig. 5a](#)).

298 Purified clay mineral samples show much stronger signals of glauconite, chamosite
299 and berthierine, but weaker signals of quartz than those in bulk rocks ([Figs. 5b–d](#)). In

300 [Figs. 5b–d](#) the intensities of basal reflection (001) of glauconite and chamosite vary,
301 indicating variable chamosite and glauconite contents in different samples, similar to
302 those of bulk rock samples.

303 The interstratifications of berthierine in chamosite have been confirmed by TEM
304 observation and calculation ([Fig. 5e and f](#)) using the method suggested by Ryan and
305 Reynolds Jr (1996). The result shows that the contents of berthierine are low (%Ber = 4.0
306 \pm 2.0%). The polytypes were also analyzed based on the method introduced by Ryan and
307 Reynolds Jr (1996), and it shows that the polytypes of the Xiamaling Ber-Ch are *Ibb*
308 rather than *Iaa*. Ten glauconite-rich samples were ethylene glycol saturated and analyzed
309 using XRD. The result shows that there is no shift in characteristic peaks of glauconite
310 when treated with ethyl glycol, indicating that the expandable layers are negligible in the
311 glauconite.

312

313 **Transformation of glauconite to chamosite**

314 **Geochemical composition of bulk rocks.** The major and trace elements of 26 bulk
315 rock samples were analyzed using HHXRF, and the results were presented in [Table S1](#)
316 and shown in [Fig. 6](#). Samples have high TFe₂O₃ concentrations of 5.41–24.12 wt% (avg.
317 17.45 wt%), which are much higher than that of PAAS (7.22 wt%, [McLennan 2001](#)) and
318 close to that of Phanerozoic ironstones (e.g., [Sturesson 2003](#)), but they have relatively
319 lower Al₂O₃ concentration of 8.56–16.18 wt% (avg. 11.30 wt%) than that of PAAS (18.90
320 wt%, [McLennan 2001](#)). Consequently, samples have high Fe/Al ratios of 0.61–3.31 (avg.
321 2.05), which is higher than those of the euxinic sediments in modern anoxic basins
322 ([Raiswell and Canfield 2012](#)). Samples are rich in V concentration (62–491 μ g/g, avg.

323 353 $\mu\text{g/g}$) and V/Al (ppm/wt%) ratio (10–81, avg. 60), higher than those of PAAS (140
324 $\mu\text{g/g}$ and 14, respectively). There is a clear positive correlation between V/Al and Fe/Al
325 (Fig. 6c).

326 There are apparent negative correlation ($R^2 = 0.66$) between K_2O and TFe_2O_3 , and
327 positive correlation ($R^2 = 0.81$) between MgO and TFe_2O_3 (Figs. 6a and 6b). These
328 compositional relationships reflect the proportional amount of glauconite and chamosite
329 in the samples: glauconite has higher K_2O , lower TFe_2O_3 and MgO contents than
330 chamosite. Increase of V/Al, TFe_2O_3 and MgO contents and decrease of K_2O correspond
331 to the increase of chamosite but decrease of glauconite in the samples (Figs. 6d–f), which
332 are consistent with the microscopic observation (Fig. 7) and XRD results (Figs. 5b–d).

333 **Microscopic features and redox-sensitive elements.** In samples with low V/Al
334 ratios, autochthonous glauconite is abundant and chamosite is minor (Fig. 7a). In samples
335 with higher V/Al ratios, more glauconite is seen to have transformed into chamosite (Figs.
336 7b–e). In samples with highest V/Al ratios, almost all glauconite was transformed into
337 chamosite (Fig. 7f).

338 **Chemical composition variations of glauconite and chamosite.** Quantitative EDS
339 was used to determine the major element compositions of glauconite and chamosite. The
340 results of 279 points are shown in Table S2 and illustrated in Fig. 8. A mixing line with
341 glauconite and chamosite as end members can be distinguished. It has been reported that,
342 in general, Precambrian glauconite has high K_2O content (Banerjee et al. 2016).
343 Therefore, particles that have $\text{K}_2\text{O} > 7.0$ wt% were identified as the glauconite
344 end-member ($n = 15$), while particles that have $\text{K}_2\text{O} = 0.0$ wt% were assigned to
345 chamosite end-member ($n = 36$). Particles that have K_2O contents of $>0.0\%$ but $<7.0\%$ (n

346 = 231) are considered as mixtures of glauconite and chamosite.

347 The glauconite end-member has higher K₂O and SiO₂, lower TFe₂O₃ and MgO
348 concentrations, and slightly lower Al₂O₃ concentrations than those of the chamosite
349 end-member (Table S2, Fig. 8). The average concentrations of K₂O, SiO₂, TFe₂O₃, MgO,
350 and Al₂O₃ are 7.21 wt% (7.01–7.58 wt%), 51.98 wt% (49.05–56.18 wt%), 15.04 wt%
351 (11.31–16.44 wt%), 2.91 wt% (2.36–3.48 wt%), and 18.39 wt% (15.94–20.27) wt%,
352 respectively; while those of the chamosite end-member are 0.00 wt%, 26.70 wt%
353 (24.72–28.81 wt%), 39.13 wt% (37.95–40.59 wt%), 6.94 wt% (5.97–8.34 wt%), and
354 21.12 wt% (19.39–22.54) wt%, respectively. Particles with compositions between the
355 glauconite and chamosite end-members along the mixing line record partial
356 transformation of glauconite to chamosite (Fig. 8). A simple calculation shows that the
357 complete transformation of glauconite to chamosite requires the addition of 16.86 wt%
358 Fe, 2.41 wt% Mg, and 1.45 wt% Al, and the loss of 11.80 wt% Si and 5.98 wt% K (Fig.
359 8).

360 Damyanov and Vassileva (2001) proposed that Mg/Fe vs. Al/Si ratio of berthierines
361 is a sensitive indicator of their geological settings. Given that chamosites were
362 transformed from berthierines under higher temperature without obvious compositional
363 change, we used the Mg/Fe–Al/Si cross plot to differentiate the geological setting of
364 chamosites. The Mg/Fe and Al/Si ratios of the examined chamosites are 0.13–0.19 and
365 0.82–0.96 (Table S2), respectively, and most of them fall into the field of marine setting
366 rather than hydrothermal origin or laterite/bauxite (Fig. 9).

367 **Ultrastructures and element mapping results.** BSE images (Fig. 10) and element
368 mappings (Fig. 11) provide further evidence for the transformation of glauconite to

369 chamosite. In BSE images, light gray chamosite is distinguishable from gray glauconite
370 and dark gray quartz (Figs. 10a). The glauconite-chamosite transformation is evident by
371 their morphological relationships: (1) light gray chamosite exists as veins irregularly
372 interspersed into glauconite particles (Figs. 10a–c); (2) light gray chamosite appears as
373 nets intertwined with gray glauconite (Fig. 10d); and (3) light gray chamosite occurs as
374 thin layers interbedded with gray glauconite layers (Figs. 10e and 10f). Newly formed
375 chamosite shares the same flakes with glauconite relics or parallel to the glauconite layers
376 (Figs. 10e and 10f). The degree of chamosite replacement varies significantly. In some
377 samples residual glauconite co-exists with newly formed chamosite (Figs. 10a–f), while
378 in others chamosite almost completely replaced glauconite (Fig. 10g). Independent of the
379 degree of transformation, newly formed quartz commonly surrounds the original
380 glauconite particles or pseudomorphs (Figs. 10a, 10d and 10g).

381 Element mapping also demonstrates the transformation of glauconite to chamosite
382 and partial quartz replacement. Due to its higher Fe but lower K and Si contents,
383 chamosite shows lighter color in the Fe element mapping and darker color in the K and Si
384 element mappings (Fig. 11). Quartz has the highest Si content and thus displays the
385 lightest color in element mappings.

386

387 **Iron speciation**

388 All together 10 samples (two mudstone, six clay-rich siltstone, and two clay-rich
389 fine sandstone) were chosen for iron speciation analysis, and the result is shown in Table
390 S3 and Fig. 12. All the samples have Fe_{py}/Fe_{HR} ratios significantly lower than 0.70 (close
391 to 0), but Fe_{HR}/Fe_T ratios ranging from 0.57 to 0.87 (>0.38), indicating ferruginous but

392 not euxinic redox conditions.

393

394

DISCUSSIONS

395 **Redox conditions of the depositional environments**

396 To determine the redox conditions of the depositional environments, the iron
397 speciation, Fe_T/Al ratios, and V/Al ratios of chamosite-bearing shales, silty mudstone,
398 clay-rich siltstone, and clay-rich fine sandstone were measured. We realized that using
399 such redox proxies in siltstone and fine-grained sandstone should be cautious because
400 detrital iron oxides may obscure seawater Fe signature. Petrographic and SEM
401 observations of the analyzed samples demonstrate that detrital components are dominated
402 by quartz, and no iron oxides or oxide pseudomorphs are observed. Thus, we consider
403 that the potential influence from detrital iron oxides, if existed, would be minor.

404 All analyzed samples have $Fe_{HR}/Fe_T > 0.38$, indicating ferruginous conditions
405 ([Raiswell and Canfield 1998](#); [Canfield et al. 2008](#)). However, Fe_{py}/Fe_{HR} values of all
406 samples are close to zero (≤ 0.1 ; [Fig. 12](#)), indicating sulfide deficiency in the depositional
407 environments. Except for two samples that have Fe/Al ratios of 0.62 and 0.96, all the
408 other samples have Fe/Al ratios > 1.0 , which are significantly higher than the average
409 value of 0.54 ± 0.11 from Phanerozoic siliciclastic rocks ([Raiswell et al. 2008](#); [Clarkson et](#)
410 [al. 2014](#)). This is consistent with Fe-rich anoxic environments ([Lyons et al. 2003](#);
411 [Clarkson et al. 2014](#)). Under anoxic environments, V enrichments are expected due to the
412 reduction of vanadyl species ([Emerson and Huested 1991](#); [Piper and Calvert 2009](#); [Zhang](#)
413 [et al. 2016](#)). Except for one sample that has the V/Al ratio close to that of PAAS
414 ($[V/Al]_{PAAS} \approx 14$ ppm/wt%), most samples have V/Al ratios of > 50 ppm/wt% ([Table S1](#)),

415 indicating significant V enrichments in anoxic environments. Collectively, Fe_{HR}/Fe_T ,
416 Fe/Al , and V/Al ratios all support anoxic and ferruginous conditions during the
417 deposition of the chamosite-bearing strata (Member-I and -II of the Xiamaling
418 Formation). The lack of Cu/Al , Ni/Al , Zn/Al and Ba/Al anomalies suggests that the
419 ferruginous conditions were not driven by local increase of primary productivity (e.g.,
420 [Tribovillard et al. 2006](#)) that could have used up oxygen and sulfate. Instead, it may
421 reflect the background seawater redox condition of the Mesoproterozoic ocean, in which
422 ferruginous conditions prevailed in response to low atmosphere oxygen (e.g., [Canfield et](#)
423 [al. 2008](#); [Planavsky et al. 2011, 2014](#); [Poulton and Canfield 2011](#); [Tang et al. 2016](#)).

424 Facies analyses suggested that the upper Member-I and Member-II of the Xiamaling
425 Formation were mainly deposited in subtidal environments below fair-weather wave base,
426 but likely above storm-weather wave base ([Gao et al. 2008a](#); [Su et al. 2008](#)). If so, it may
427 imply that, during the deposition of the chamosite-bearing strata, the redoxcline was
428 possibly shallow and close to the fair-weather wave base.

429

430 **Glauconite-chamosite transformation models**

431 Berthierine (chamosite) can be formed through diagenetic recrystallization of many
432 different precursors, such as glauconite, odinite, kaolinite and iron-oxide (hydroxide), or
433 others in marine-influenced environments ([Odin et al. 1988](#); [Drits et al. 2001](#); [Fu et al.](#)
434 [2015](#); [Kozłowska and Maliszewska 2015](#); [Mu et al. 2015](#)). In this study, microscopic
435 observation, SEM, EDS and XRD results all indicate that chamosite was transformed
436 from glauconite. Morphologically, the transformation from glauconite to chamosite did
437 not change the size and shape of the original glauconite particles ([Fig. 4e](#)) and the newly

438 formed chamosite shares the flakes with glauconite relics or parallels to the glauconite
439 layers (Figs. 10e and 10f). This implies that the glauconite-chamosite phase
440 transformation was not accompanied by intense dissolution and growth of crystals from
441 fluids (e.g., Mu et al. 2015). Such morphological features seem to support mainly
442 solid-state formation of chamosite crystallites from glauconite (e.g., Drits et al. 2001),
443 although partial dissolution and precipitation are permitted at immediate stages of the
444 transformation. Geochemically, a complete transformation of glauconite to chamosite
445 requires not only the addition of significant amounts of Fe^{2+} and Mg^{2+} and a lesser
446 amount of Al^{3+} , but also a simultaneous release of a large amount of Si and K (Figs. 6 and
447 8).

448 There are currently two models for the transformation of glauconite to chamosite.
449 One model emphasizes that glauconite transforms to chamosite without an intermediate,
450 and the other suggests that glauconite first transforms to berthierine and then to
451 chamosite during deeper burial (Drits et al. 2001). The first model requires a high
452 transformation temperature ($>175^\circ\text{C}$, Drits et al. 2001), which seems to contradict with
453 the low temperature estimation ($\leq 90^\circ\text{C}$) for the Xiamaling shales based on the thermal
454 maturity of organic matter (Zhang et al. 2016). In addition, at burial depths reaching a
455 temperature of $>175^\circ\text{C}$, porewater Fe^{2+} and Mg^{2+} would not be available. Unless there
456 were significant external Fe^{2+} and Mg^{2+} inputs from formation fluids or hydrothermal
457 fluids, a direct transformation from glauconite to chamosite requires Fe^{2+} and Mg^{2+}
458 sources from iron-rich minerals adjacent to glauconite particles, which has not been
459 observed in our samples. Hydrothermal alteration is not supported by the lack of bedding
460 disruption in glauconite-chamosite rich layers and by elevated Mg/Fe ratios higher than

461 those of hydrothermal chamosite (Fig. 9).

462 The presence of $4.0\pm 2.0\%$ interstratification of berthierine in chamosite (Fig. 5e)
463 supports the second model that involves a berthierine intermediate during
464 glauconite-chamosite transformation (Drits et al. 2001). Berthierine is a low temperature
465 mineral that forms at $25\text{--}45^\circ\text{C}$ (Hornibrook and Longstaffe 1996) during early diagenesis,
466 when ion exchange between porewater and seawater is still available. The required Fe^{2+}
467 and Mg^{2+} for transformation from glauconite to berthierine could be readily supplied by
468 ferruginous seawater at or near the seawater/sediment interface. Subsequent transfer from
469 berthierine to chamosite at higher temperature ($\geq 70^\circ\text{C}$) does not involve much
470 compositional change. Since the glauconite-berthierine transformation temperature is low
471 ($\leq 45^\circ\text{C}$), only minor berthierine can be retained during deeper burial (Fig. 5; Hornibrook
472 and Longstaffe 1996).

473 To maintain a fixed volume from glauconite to berthierine, two processes may have
474 involved. The first process involves the removal of interlayer cations and one tetrahedral
475 sheet of the 2:1 layer, and the occupation of vacant octahedra by Mg^{2+} and Fe^{2+} cations
476 adsorbed from porewater (Fig. 13a). However, such a process would result in significant
477 decrease in crystal volume. Thus, it requires the second process: the removal of interlayer
478 cations is accompanied by the inversion of upper tetrahedral sheets of 2:1 layers, which,
479 together with Mg^{2+} and Fe^{2+} cations extracted from solution, produce berthierine layers.
480 Such a reaction would result in the substitution of a 2:1 layer by two 1:1 layers (Fig. 13b),
481 increasing the volume of the primary crystallites. The subsequent transfer from
482 berthierine to chamosite at higher temperature is proceeded with solid-state
483 transformation by the inversion of tetrahedral sheets of the even 1:1 layers (Fig. 13c). The

484 incompleteness of this process results in the remaining of minor berthierine (Figs. 5e and
485 f).

486

487 **Environmental control on glauconite-chamosite transformation**

488 Compared with Phanerozoic glauconite that has high TFe_2O_3 content (commonly >
489 20 wt%), most Precambrian glauconies have low TFe_2O_3 contents (commonly < 15 wt%;
490 Banerjee et al. 2015, 2016), which was possibly controlled by weakly oxygenated
491 Precambrian seawater and the dioctahedral structure of glauconite (Tang et al. 2017). In
492 this study the average Fe content of the glauconite end-member is 10.53 wt%, while the
493 average Fe content of the chamosite end-member is 27.39 wt% (Fig. 8). That means that
494 a significant amount of Fe is needed during the glauconite-chamosite transformation.
495 Potential Fe sources may include iron-bearing freshwater (Odin and Matter 1981;
496 Kozłowska and Maliszewska 2015), hydrothermal fluids, iron-rich detrital minerals (e.g.,
497 iron oxides and biotite), or Fe-rich seawater. The Fe source from freshwater can be
498 excluded, because freshwater commonly contains less Mg^{2+} and K^+ in comparison with
499 seawater, which is not favored for glauconite formation. The Fe source from
500 hydrothermal fluids can also be excluded, because the glauconite- and chamosite-bearing
501 layers are thick (~20 m) and spatially stable in the Xiamaling Formation across the North
502 China Platform, from which no nearby intrusive rocks or hydrothermal fluid conduits
503 have been observed. Thin, laterally discontinuous diabases are indeed locally present in
504 the Xiamaling Formation, but they are mainly concentrated in shales (Fig. 1a) from
505 which no chamosite is found. In the Mg/Fe–Al/Si cross plot, almost all chamosites fall
506 into the area of marine origin (Fig. 9). In all the studied samples, detrital Fe-rich minerals

507 such as biotite and iron oxides are rare and the Fe₂O₃ contents are independent of Al₂O₃
508 (Table S1). Therefore, Fe-rich detrital minerals seem not to be a significant Fe source.

509 Because the glauconite-chamosite transformation requires Fe²⁺, rather than Fe³⁺, the
510 most likely Fe²⁺ source would be ferruginous seawater. During early diagenesis when
511 porewater and ferruginous seawater are exchangeable or partially exchangeable, Fe²⁺
512 supply is unlimited, providing sufficient Fe²⁺ needed for the transformation of glauconite
513 to berthierine, which further changes to chamosite during deeper burial (Drits et al. 2001).
514 This is consistent with the ferruginous water-column conditions suggested by Fe
515 speciation, Fe/Al ratios and V/Al ratios. Thus, from the viewpoint of mineralogy, the
516 presence of abundant chamosite (or berthierine) in sedimentary successions may be used
517 as an indicator for ferruginous seawater, if the other sources of Fe can be excluded.

518

519

IMPLICATIONS

520 Integrated petrographic, mineralogical, and geochemical study of the Fe-rich clay
521 minerals (glauconite, berthierine, and chamosite) from the Mesoproterozoic Xiamaling
522 Formation (~1.40–1.35 Ga) reveals information about the paleoenvironmental control on
523 clay mineral transformation. Chamosites from the Xiamaling Formation either mimic the
524 outlines of glauconite particles or partially replace glauconite, indicating
525 glauconite-chamosite mineral transformation. The low thermal maturity of organic matter
526 from hosting rocks ($\leq 90^\circ\text{C}$) and the presence, although rare, of berthierine relics suggest
527 that the glauconite-chamosite transformation was proceeded with an intermediate
528 berthierine mineral phase. The compositional change mainly happened during the
529 glauconite-berthierine transformation at low temperature (25–45°C); subsequent transfer

530 from berthierine to chamosite at higher temperature ($\geq 70^\circ\text{C}$) does not involve much
531 compositional change.

532 The mineral transformation from glauconite to berthierine requires constant Fe^{2+}
533 supply from iron-bearing freshwater, hydrothermal fluids, iron-rich detrital minerals, or
534 iron-rich seawater. The presence of glauconite (not favorable for freshwater), the absence
535 of detrital Fe-rich minerals (e.g., biotite and iron oxides) in studied samples, and the lack
536 of evidence for hydrothermal alteration in the hosting strata suggest that the required Fe^{2+}
537 may have been from Fe^{2+} -rich (ferruginous) seawater, which could have promoted
538 glauconite-berthierine transformation at the very early diagenetic stage when Fe^{2+}
539 exchange between pore-water and seawater was still available. This is consistent with the
540 high $\text{Fe}_{\text{HR}}/\text{Fe}_{\text{T}}$ (but low $\text{Fe}_{\text{py}}/\text{Fe}_{\text{HR}}$), Fe/Al , and V/Al ratios from the hosting strata that
541 support ferruginous depositional environments. Thus, the abundance of berthierine (or
542 chamosite in deeper burial) in fine-grained, marine siliciclastic sediments may be used as
543 a mineral indicator of ferruginous water-column conditions, if the other sources of Fe can
544 be excluded.

545

546 ACKNOWLEDGMENTS

547 The study was supported by the National Natural Science Foundation of China (Nos.
548 41672336 and 41402024). We thank Jianbai Ma for field assistance and sample
549 preparation, Yong Han for her kind help in TEM analysis. We thank Dr. Warren Huff
550 (Editor), Dr. Peter Ryan and an anonymous reviewer for their constructive comments that
551 helped to improve the paper.

552

553

REFERENCES CITED

- 554 Banerjee, S., Mondal, S., Chakraborty, P.P., and Meena, S.S. (2015) Distinctive
555 compositional characteristics and evolutionary trend of Precambrian glaucony:
556 Example from Bhalukona Formation, Chhattisgarh basin, India. *Precambrian
557 Research*, 271, 33–48.
- 558 Banerjee, S., Bansal, U., and Thorat, A. (2016) A review on palaeogeographic
559 implications and temporal variation in glaucony composition. *Journal of
560 paleogeography*, 5, 43–71.
- 561 Bhattacharyya, D.P. (1983) Origin of berthierine in ironstones. *Clays and Clay Minerals*,
562 31, 173–182.
- 563 Canfield, D.E., Raiswell, R., Westrich, J.T., Reaves, C.M., and Berner, R.A. (1986) The
564 use of chromium reduction in the analysis of reduced inorganic sulfur in sediments
565 and shales. *Chemical Geology*, 54, 149–155.
- 566 Canfield, D.E., Poulton, S.W., Knoll, A.H., Narbonne, G.M., Ross, G., Goldberg, T., and
567 Strauss, H. (2008) Ferruginous conditions dominated later Neoproterozoic
568 deepwater chemistry. *Science*, 321, 949–952.
- 569 Clarkson, M.O., Poulton, S.W., Guilbaud, R., and Wood, R.A. (2014) Assessing the
570 utility of Fe/Al and Fe-speciation to record water column redox conditions in
571 carbonate-rich sediments. *Chemical Geology*, 382, 111–122.
- 572 Damyanov, Z., and Vassileva, M. (2001) Authigenic phyllosilicates in the Middle Triassic
573 Kremikovtsi sedimentary exhalative siderite iron formation, Western Balkan,
574 Bulgaria. *Clays and Clay Minerals*, 49, 559–585.
- 575 Dai, S., and Chou, C.L. (2007) Occurrence and origin of minerals in a chamosite-bearing

- 576 coal of Late Permian age, Zhaotong, Yunnan, China. *American Mineralogist*, 92,
577 1253–1261.
- 578 Drits, V.A., Ivanovskaya, T.A., Sakharov, B.A., Gor'kova, N.V., Karpova, G.V., and
579 Pokrovskaya, E.V. (2001) Pseudomorphous Replacement of Globular Glauconite
580 by Mixed-Layer Chlorite–Berthierine in the Outer Contact of Dike: Evidence from
581 the Lower Riphean Ust'-Il'ya Formation, Anabar Uplift. *Lithology and Mineral
582 Resources*, 36, 337–352.
- 583 Duan, C., Li, Y.H., Wei, M.H., Yang, Y., Hou, K.J., Chen, X.D., and Zhou, B. (2014)
584 U-Pb dating study of detrital zircons from the Chuanlinggou Formation in
585 Jiangjiazhai iron deposit, North China Craton and its geological significances. *Acta
586 Petrologica Sinica*, 30, 35–48 (in Chinese with English abstract).
- 587 Emerson, S.R., and Huested, S.S. (1991) Ocean anoxia and the concentrations of
588 molybdenum and vanadium in seawater. *Marine Chemistry*, 34, 177–196.
- 589 Evans D.A.D., and Mitchell, R.N. (2011) Assembly and breakup of the core of
590 Paleoproterozoic-Mesoproterozoic supercontinent Nuna. *Geology*, 39: 443–446.
- 591 Fritz, S.J., and Toth, T.A. (1997) An Fe-berthierine from a Cretaceous laterite: part II.
592 Estimation of Eh, pH and $p\text{CO}_2$ conditions of formation. *Clays and Clay Minerals*,
593 45, 590–586.
- 594 Fu, Y., Berk, W.V., Schulz, H.M., and Mu, N. (2015) Berthierine formation in reservoir
595 rocks from the Siri oilfield (Danish North Sea) as result of fluid–rock interactions:
596 part II. Deciphering organic–inorganic processes by hydrogeochemical modeling.
597 *Marine and Petroleum Geology*, 65, 317–326.
- 598 Gao, L.Z., Zhang, C.H., Shi, X.Y., Zhou, H.R., and Wang, Z.Q. (2007) Zircon SHRIMP

- 599 U-Pb dating of the tuff bed in the Xiamaling Formation of the Qingbaikouan System
600 in North China. *Geological Bulletin of China*, 26, 249–255 (in Chinese with English
601 abstract).
- 602 Gao, L.Z., Zhang, C.H., Shi, X.Y., Song, B., Wang, Z.Q., and Liu, Y.M. (2008a)
603 Mesoproterozoic age for Xiamaling Formation in North China plate indicated by
604 zircon SHRIMP dating. *Chinese Science Bulletin*, 53, 2665–2671.
- 605 Gao, L.Z., Zhang, C.H., Yin, C.Y., Shi, X.Y., Wang, Z.Q., Liu, Y.M., Liu, P.J., Tang, F.,
606 and Song, B. (2008b) SHRIMP zircon ages: basis for refining the
607 chronostratigraphic classification of the Meso- and Neoproterozoic strata in North
608 China old land. *Acta Geoscientica Sinica*, 29, 366–376 (in Chinese with English
609 abstract).
- 610 Gao, L.Z., Zhang, C.H., Liu, P.J., Ding, X.Z., Wang, Z.Q., and Zhang, Y.J. (2009)
611 Recognition of Meso- and Neoproterozoic stratigraphic framework in North and
612 South China. *Acta Geoscientica Sinica*, 30, 433–446 (in Chinese with English
613 abstract).
- 614 Hornibrook, E.R.C., and Longstaffe, F.J. (1996) Berthierine from the Lower Cretaceous
615 Clearwater Formation, Alberta, Canada. *Clays and Clay Minerals*, 44, 1–21.
- 616 Iijima, A., and Matsumoto, R. (1982) Berthierine and chamosite in coal measures of
617 Japan. *Clays and Clay Minerals*, 30, 264–274.
- 618 Kozłowska, A., and Maliszewska, A. (2015) Berthierine in the Middle Jurassic sideritic
619 rocks from southern Poland. *Geological Quarterly*, 59, 551–564.
- 620 Li, X.H., Li, W.X., Li, Z.X., and Liu, Y. (2008) 850–790 Ma bimodal volcanic and
621 intrusive rocks in northern Zhejiang, South China: a major episode of continental rift

- 622 magmatism during the breakup of Rodinia. *Lithos*, 102, 341–357.
- 623 Li, H.K., Zhu, S.X., Xiang, Z.Q., Su, W.B., Lu, S.N., Zhou, H.Y., Geng, J.Z., Li, S., and
624 Yang, F.J. (2010) Zircon U-Pb dating on tuff bed from Gaoyuzhuang formation in
625 Yanqing, Beijing: further constraints on the new subdivision of the Mesoproterozoic
626 stratigraphy in the northern North China Craton. *Acta Petrologica Sinica*, 2,
627 2131–2140 (in Chinese with English abstract).
- 628 Li, H.K., Lu, S.N., Su, W.B., Xiang, Z.Q., Zhou, H.Y., and Zhang, Y.Q. (2013) Recent
629 advances in the study of the Mesoproterozoic geochronology in the North China
630 Craton. *Journal of Asian Earth Sciences*, 72, 216–227.
- 631 Li, H.K., Su, W.B., Zhou, H.Y., Xiang, Z.Q., Tian, H., Yang, L.G., Huff, W.D., and
632 Ettensohn, F.R. (2014) The first precise age constraints on the Jixian System of the
633 Meso- to Neoproterozoic Standard Section of China: SHRIMP zircon U–Pb dating
634 of bentonites from the Wumishan and Tieling formations in the Jixian Section, North
635 China Craton. *Acta Petrologica Sinica*, 30, 2999–3012.
- 636 Lu, S.N., and Li, H.M. (1991) A precise U-Pb single zircon age determination for the
637 volcanics of Dahongyu Formation, Changcheng system in Jixian. *Acta Geoscientia*
638 *Sinica*, 22, 137–145 (in Chinese with English abstract).
- 639 Lu, S.N., Zhao, G.C., Wang, H.C., and Hao, G.J. (2008) Precambrian metamorphic
640 basement and sedimentary cover of the North China Craton: a review. *Precambrian*
641 *Research*, 160, 77–93.
- 642 Lyons, T.W., Werne, J.P., Hollander, D.J., Murray, R.W. (2003) Contrasting sulfur
643 geochemistry and Fe/Al and Mo/Al ratios across the last oxic-to-anoxic transition in
644 the Cariaco basin, Venezuela. *Chemical Geology*, 195, 131–157.

- 645 Ma, L.F., Qiao, X.F., Ming, L.R., Fan, B.X., and Ding, X.Z. (2002) Atlas of Geological
646 Maps of China, 348 p. Geological Press, Beijing (in Chinese).
- 647 McLennan, S.M. (2001) Relationships between the trace element composition of
648 sedimentary rocks and upper continental crust. *Geochemistry Geophysics*
649 *Geosystems*, 2, 203–236.
- 650 Meng, Q.R., Wei, H.H., Qu, Y.Q., and Ma, S.X. (2011) Stratigraphic and sedimentary
651 records of the rift to drift evolution of the northern North China Craton at the Paleo-
652 to Mesoproterozoic transition. *Gondwana Research*, 20, 205–218.
- 653 Mu, N., Schulz, H.M., Fu, Y., Schovsbo, N.H., Wirth, R., Rhede, D., and van Berk, W.
654 (2015) Berthierine formation in reservoir rocks from the Siri oilfield (Danish North
655 Sea) as result of fluid-rock interactions: Part I. Characterization. *Marine and*
656 *Petroleum Geology*, 30, 302–316.
- 657 Odin, G.S., and Matter, A. (1981) De glauconiarum origine. *Sedimentology*, 28, 611–641.
- 658 Odin, G.S., Knox R.W.O'B., Gygi, R.A., and Guerrak, S. (1988) Green marine clays from
659 the oolitic ironstone facies. *Developments in Sedimentology*, 45, 29–52.
- 660 Piper, D.Z., and Calvert, S.E. (2009). A marine biogeochemical perspective on black
661 shale deposition. *Earth-Science Reviews*, 95, 63–96.
- 662 Planavsky, N.J., McGoldrick, P., Scott, C.T., Li, C., Reinhard, C.T., Kelly, A.E., Chu, X.,
663 Bekker, A., Love, G.D., and Lyons, T.W., (2011) Widespread iron-rich conditions in
664 the mid-Proterozoic ocean. *Nature*, 477, 448–451.
- 665 Planavsky, N.J., Reinhard, C.T., Wang, X.L., Thomson, D., McGoldrick, P., Rainbird, R.
666 H., Johnson, T., Fischer, W.W., Lyons, T.W. (2014) Low Mid-Proterozoic
667 atmospheric oxygen levels and the delayed rise of animals. *Science*, 346, 635–638.

- 668 Poulton, S.W., and Canfield, D.E. (2005) Development of a sequential extraction
669 procedure for iron: implications for iron partitioning in continentally derived
670 particulates. *Chemical Geology*, 214, 209–221.
- 671 Poulton, S.W., and Canfield, D.E. (2011) Ferruginous conditions: a dominant feature of
672 the ocean through earth's history. *Elements*, 7, 107–112.
- 673 Raiswell, R., and Canfield, D.E. (1998) Sources of iron for pyrite formation in marine
674 sediments. *American Journal of Science*, 298, 219–245.
- 675 Raiswell, R., Newton, R., Bottrell, S.H., Coburn, P.M., Briggs, D.E., Bond, D.P., and
676 Poulton, S.W. (2008) Turbidite depositional influences on the diagenesis of
677 Beecher's Trilobite Bed and the Hunsrück Slate; sites of soft tissue pyritization.
678 *American Journal of Science*, 308, 105–129.
- 679 Raiswell, R., and Canfield, D.E. (2012) The iron biogeochemical cycle past and present.
680 *Geochemical Perspectives*, 1, 1–220.
- 681 Reynolds, R.C., DiStefano, M.P., and Lahann, R.W. (1992) Randomly interstratified
682 serpentine/chlorite: Its detection and quantification by powder X-ray diffraction
683 methods. *Clays and Clay Minerals*, 40, 262–262.
- 684 Rivard, C., Pelletier, M., Michau, N., Razafitianamaharavo, A., Bihannic, I., Abelmoula,
685 M., Ghanbaja, J., and Villieras, F. (2013) Berthierine-like mineral formation and
686 stability during the interaction of kaolinite with metallic iron at 90°C under anoxic
687 and oxic conditions. *American Mineralogist*, 98, 163–180.
- 688 Rivas-Sanchez, M.L., Alva-Valdivia, L.M., Arenas-Alatorre, J., Urrutia-Fucugauchi, M.,
689 Ruiz-Sandoval, M., and Ramos-Molina, M.A. (2006) Berthierine and chamosite
690 hydrothermal: genetic guides in the Pena Colorada magnetite-bearing ore deposit,

- 691 Mexico. *Earth Planets Space*, 58, 1389–1400.
- 692 Ryan, P.C., and Hillier, S. (2002) Berthierine/chamosite, corrensite, and discrete chlorite
693 from evolved verdine and evaporate-associated facies in the Jurassic Sundance
694 Formation, Wyoming. *American Mineralogist*, 87, 1607–1615.
- 695 Ryan, P.C., and Reynolds Jr., R.C. (1996) The origin and diagenesis of grain-coating
696 serpentine-chlorite in Tuscaloosa Formation sandstone, US Gulf Coast. *American*
697 *Mineralogist*, 81, 213–225.
- 698 Sheldon, N.D., and Retallack, G.J. (2002) Low oxygen levels in earliest Triassic soils.
699 *Geology*, 30, 919–922.
- 700 Sturesson, U. (2003) Lower Palaeozoic iron oolites and volcanism from a Baltoscandian
701 perspective. *Sedimentary Geology*, 159, 241–256.
- 702 Su, W.B., Zhang, S.H., Huff, W.D., Li, H.K., Ettensohn, F.R., Chen, X.Y., Yang, H.M.,
703 Han, Y.G., Song, B., and Santosh, M. (2008) SHRIMP U–Pb ages of K-bentonite
704 beds in the Xiamaling Formation: implications for revised subdivision of the
705 Meso-to Neoproterozoic history of the North China Craton. *Gondwana Research*, 14,
706 543–553.
- 707 Su, W.B., Li, H.K., Huff, W.D., Ettensohn, F.R., Zhang, S.H., Zhou, H.Y., and Wan, Y.S.
708 (2010) SHRIMP U-Pb dating for a K-bentonite bed in the Tieling Formation, North
709 China. *Chinese Science Bulletin*, 55, 3312–3323.
- 710 Su, W.B. (2014) A review of the revised Precambrian time scale (GTS2012) and the
711 research of the Mesoproterozoic chronostratigraphy of China. *Earth Science*
712 *Frontiers*, 21, 119–138.
- 713 Su, W.B. (2016) Revision of the Mesoproterozoic chronostratigraphic subdivision both of

- 714 North China and Yangtze Cratons and the relevant issues. *Earth Science Frontiers*,
715 23, 156–185.
- 716 Tang, D.J., Shi, X.Y., Liu, D.B., Lin, Y.T., Zhang, C.H., and Song, G.Y., Wu, J.J. (2015)
717 Terminal paleoproterozoic ooidal ironstone from North China: a sedimentary
718 response to the initial breakup of Columbia supercontinent. *Earth Science—Journal*
719 *of China University of Geosciences*, 40, 290–304.
- 720 Tang D.J., Shi, X.Y., Wang, X.Q., and Jiang, G.Q. (2016) Extremely low oxygen
721 concentration in mid-Proterozoic shallow seawaters. *Precambrian Research*, 276,
722 145–157.
- 723 Tang, D.J., Shi, X.Y., Ma, J.B., Jiang, G.Q., Zhou, X.Q, Shi, Q. (2017) Formation of
724 shallow-water glaucony in weakly oxygenated Precambrian ocean: An example
725 from the Mesoproterozoic Tieling Formation in North China. *Precambrian Research*,
726 294, 214–229.
- 727 Taylor, K.G. (1990) Berthierine from the non-marine Wealden (Early Cretaceous)
728 sediments of south-east England. *Clay Minerals*, 25, 391–399.
- 729 Taylor, K.G., and Curtis, C.D. (1995) Stability and facies association of early diagenetic
730 mineral assemblages: an example from a Jurassic iron stone-mudstone succession,
731 U.K. *Journal of Sedimentary Research*, A65: 358–368.
- 732 Taylor, K.G., Simo, T.J.A., Yocum, D., and Leckie, D.A. (2002) Stratigraphic significance
733 of ooidal ironstone from the Cretaceous western interior seaway: the Peace River
734 Formation, Alberta, Canada, and the Castlegate Sandstone, Utah, U.S.A. *Journal of*
735 *Sedimentary Research*, 72, 316–327.
- 736 Tian, H., Zhang, J., Li, H.K., Su, W.B., Zhou, H.Y., Yang, L.G., Xiang, Z.Q., Geng, J.Z.,

- 737 Liu, H., Zhu, S.X., and Xu, Z.Q. (2015) Zircon LA-MC-ICPMS U–Pb dating of tuff
738 from Mesoproterozoic Gaoyuzhuang Formation in Jixian County of North China
739 and its geological significance. *Acta Geoscientica Sinica*, 36, 647–658.
- 740 Tribovillard, N., Algeo, T.J., Lyons, T., and Riboulleau, A. (2006) Trace metals as
741 paleoredox and paleoproductivity proxies: an update. *Chemical geology*, 232,
742 12–32.
- 743 Velde, B. (1995) *Origin and Mineralogy of Clays: Clays and Environment*, 334 p.
744 Springer, Verlag.
- 745 Wang, H.Z., Chu, X.C., Liu, B.P., Hou, H.F., and Ma, L.F. (1985) *Atlas of the*
746 *Palaeogeography of China*, 143 p. Cartographic Publishing House, Beijing (in
747 Chinese and English).
- 748 Wang, H.Z., Shi, X.Y., Wang, X.L., Yin, H.F., Qiao, X.F., Liu, B.P., Li, S.T., and Chen,
749 J.Q. (2000) *Research on the Sequence Stratigraphy of China*, 457 p. Guangdong
750 Science and Technology Press, Guangzhou (in Chinese).
- 751 Worden, R.H., and Morad, S. (2003) Clay minerals in sand stones: controls on formation,
752 distribution and evolution. In: R.H. Worden and S. Morad Eds., *Clay Mineral*
753 *Cements in Sandstones*, 34, p. 3–41. International Association of Sedimentologists
754 Special Publication, Blackwell Publishing, Oxford.
- 755 Young, T.P., and Taylor, W.E.G., Eds (1989) *Phanerozoic Ironstones*, 251p. Geological
756 Society Special Publications, London.
- 757 Zhang, S.H., Zhao, Y., Yang, Z.Y., He, Z.F., and Wu, H. (2009) The 1.35Ga diabase sills
758 from the Northern North China Craton: implications for breakup of the Columbia
759 (Nuna) supercontinent. *Earth and Planetary Science Letters*, 288, 588–600.

- 760 Zhang, S.H., Zhao, Y., and Santosh, M. (2011) Mid-Mesoproterozoic bimodal magmatic
761 rocks in the northern North China Craton: implications for magmatism related to
762 breakup of the Columbia supercontinent. *Precambrian Research*, 222, 339–367.
- 763 Zhang, S.H., Li, Z.X., Evans, D.A.D., Wu, H.C., Li, H.Y., and Dong, J. (2012)
764 Pre-Rodinia supercontinent Nuna shaping up: A global synthesis with new
765 paleomagnetic results from North China. *Earth and Planetary Science Letters*, 353,
766 145–155.
- 767 Zhang, S.H., Zhao, Y., Ye, H., Hu, J.M., and Wu, F. (2013) New constraints on ages of the
768 Chuanlinggou and Tuanshanzi formations of the Changcheng System in the
769 Yan-Liao area in the northern North China Craton. *Acta Petrologica Sinica*, 29,
770 2481–2490.
- 771 Zhang, S.H., Zhao, Y., Li, X., Ernst, R.E., and Yang, Z. (2017) The 1.33–1.30 Ga Yanliao
772 large igneous province in the North China Craton: Implications for reconstruction of
773 the Nuna (Columbia) supercontinent, and specifically with the North Australian
774 Craton. *Earth and Planetary Science Letters*, 465, 112–125.
- 775 Zhang, S.C., Wang, X.M., Hammarlund, E.U., Wang, H.J., Costa, M.M., Bjerrum, C.J.,
776 Connelly, J.N., Zhang, B.M., Bian, L.Z., and Canfield, D.E. (2015) Orbital forcing
777 of climate 1.4 billion years ago. *Proceedings of the National Academy of Sciences*,
778 112, E1406–E1413.
- 779 Zhang, S.C., Wang, X.M., Wang, H.J., Bjerrum, C.J., Hammarlund, E.U., Costa, M.M.,
780 Connelly, J.N., Zhang, B.M., Su, J., and Canfield, D.E. (2016) Sufficient oxygen for
781 animal respiration 1,400 million years ago. *Proceedings of the National Academy of*
782 *Sciences*, 113, 1731–1736.

- 783 Zhao, G.C., Sun, M., Wilde, S.A., and Li, S.Z. (2003) Assembly, accretion and breakup of
784 the Paleo-Mesoproterozoic Columbia supercontinent: records in the North China
785 Craton. *Gondwana Research*, 6, 417–434.
- 786 Zhao, G.C., Sun, M., Wilde, S.A., and Li, S.Z. (2004) A Paleo-Mesoproterozoic
787 supercontinent: assembly, growth and breakup. *Earth-Science Reviews*, 67, 91–123.
- 788 Zhao, G.C., Li, S.Z., Sun, M., and Wilde, S.A. (2011) Assembly, accretion, and break-up
789 of the Palaeo-Mesoproterozoic Columbia supercontinent: records in the North China
790 Craton revisited. *International Geology Review*, 53, 1331–1356.
- 791 Zhao, L., Dai, S., Graham, I.T., and Wang, P. (2016) Clay Mineralogy of Coal-Hosted
792 Nb-Zr-REE-Ga Mineralized Beds from Late Permian Strata, Eastern Yunnan, SW
793 China: Implications for Paleotemperature and Origin of the Micro-Quartz. *Minerals*,
794 6, 45, doi:10.3390/min6020045
- 795 Zhou, H.R., Mei, M.X., Luo, Z.Q., and Xing, K. (2006) Sedimentary sequence and
796 stratigraphic framework of the Neoproterozoic Qingbaikou system in the Yanshan
797 region, North China. *Earth Science Frontiers*, 13, 280–290 (in Chinese with English
798 abstract).

799

800

FIGURE CAPTIONS

801 **Figure 1.** (a) Stratigraphic succession of the Xiamaling Formation at Zhaojiashan,
802 Huailai, Hebei Province. (b) Major tectonic subdivisions of China. The box shows the
803 area illustrated in [Fig. 1c](#). (c) Mesoproterozoic paleogeographic map of the central North
804 China platform, modified after Wang et al. (1985). (d) Simplified geological map of the
805 study area, modified after Ma et al. (2002).

806

807 **Figure 2.** Lithostratigraphic subdivisions of the Proterozoic succession in the North
808 China platform and their age constraints (Age data adopted from [Lu and Li 1991](#); [Gao et](#)
809 [al. 2008a, 2008b](#); [Lu et al. 2008](#); [Su et al. 2008, 2010](#); [Li et al. 2010, 2014](#); [Zhang et al.](#)
810 [2013, 2015](#); [Duan et al. 2014](#); [Tian et al. 2015](#)).

811

812 **Figure 3.** Field photographs showing major depositional facies of the Xiamaling
813 Formation. (a) Gray to greenish silty shale interbedded with argillaceous siltstone in
814 Member-I of the Xiamaling Formation. (b) Siderite-concretion in silty shale of Member-I
815 of the Xiamaling Formation. (c) Gravely muddy sandstone at the basal Xiamaling
816 Formation. (d) Greenish siltstone–argillaceous sandstone in Member-II of the Xiamaling
817 Formation. (e) Close view of the greenish siltstone–argillaceous sandstone in Member-II
818 of the Xiamaling Formation. (f) Purplish shale alternated with greenish shale and light
819 colored ankerite-rich carbonate lenticles in Member-II of the Xiamaling Formation. (g)
820 Greenish shale with purplish shale interbeds in Member-II of the Xiamaling Formation.
821 (h) Black shale in Member-III of the Xiamaling Formation.

822

823 **Figure 4.** Photomicrographs showing microfacies and occurrences of glauconite and
824 chamosite in the Xiamaling Formation. (a) Glauconite- and chamosite-bearing siltstone.
825 (b) Glauconite-bearing argillaceous sandstone, showing autochthonous glauconite (green,
826 partially transformed into chamosite) with irregular outlines. (c) Photomicrograph with
827 high magnification, showing autochthonous glauconite with irregular outlines. (d) Green
828 glauconite-rich particle with obvious diagenetic compaction, while yellowish-green

829 chamosite-rich particles without perceptible diagenetic compaction. (e) Subrounded
830 chamosite (arrows) with some glauconite relics. (f and g) Photomicrographs under plain
831 (f) and cross polarized (g) light, showing autochthonous glauconite-bearing sandstone
832 composed mainly of chert, quartz and glauconite, and minor pyrite. (h) Photomicrographs
833 under cross polarized light, showing autochthonous chamosite-bearing sandstone
834 composed mainly of chert, quartz and chamosite.

835

836 **Figure 5.** X-ray pattern of bulk rocks and purified clay minerals. (a) Three X-ray patterns
837 of selected samples with varied chamosite and glauconite contents, indicated by their
838 different basal reflection (001) intensities of chamosite (1.429 nm) and glauconite (1.014
839 nm). (b–d) X-ray patterns of purified clay minerals, showing increasing basal reflection
840 (001) intensities of chamosite while decreasing basal reflection (001) intensities of
841 glauconite from Fig. 5b to Fig. 5d; minor berthierine (basal reflection at 0.466 nm) and
842 kaolinite (basal reflection at 0.447 nm) are identifiable. (e) The 004 and 005 peaks of
843 Berthierine-Chamosite. (f) Randomly oriented XRD patterns of *Ibb-Iaa* polytypes
844 showing obvious *Ibb* (204) peak but negligible *Ibb* (204) peak. (g) TEM images of
845 berthierine-chamosite interstratification showing lattice fringes with ~0.70 nm and ~1.40
846 nm periodicities, respectively. (h) XRD result of air dried and glycol saturated sample,
847 showing that there is no shift of characteristic peaks of glauconite when treated with ethyl
848 glycol. C (Ch) = chamosite, G = glauconite, B (Ber) = berthierine, K = kaolinite, Q =
849 quartz, A = albite.

850

851 **Figure 6.** Bulk rock element compositions of glauconite- and chamosite-bearing samples.

852 The relative abundance of chamosite and glauconite in these samples is determined by
853 petrographic observations as shown in Fig. 7. (a) Cross plot of K_2O vs. TFe_2O_3 , showing
854 that the transformation from glauconite to chamosite requires the addition of Fe but loss
855 of K. (b) Cross plot of MgO vs. TFe_2O_3 , showing that the transformation of glauconite to
856 chamosite requires the addition of Fe and Mg. (c) Cross plot of V/Al vs. Fe/Al, showing a
857 positive correlation between V/Al and Fe/Al. (d) Cross plot of TFe_2O_3 vs. V/Al, showing
858 the positive correlation between V/Al and TFe_2O_3 , with higher V/Al ratios in
859 chamosite-rich samples. (e) Cross plot of K_2O vs. V/Al, showing a reverse correlation
860 between V/Al ratios and K_2O contents (glauconite). (f) Cross plot of MgO vs. V/Al,
861 showing positive correlation between V/Al ratios and MgO contents (chamosite).

862

863 **Figure 7.** Microscopic features recording the transformation from glauconite to
864 chamosite in siltstone-argillaceous sandstone with variable V/Al values. (a) An
865 argillaceous sandstone sample with the lowest V/Al value, containing the most amount of
866 autochthonous glauconite but minimum chamosite. (b and c) Siltstone-argillaceous
867 sandstones with relatively low V/Al values, containing significant amount of chamosite
868 but minor amount of glauconite. (d and e) Argillaceous sandstones with relatively high
869 V/Al values, containing large amount of chamosite but minor glauconite that has been
870 partially transformed into chamosite. (f) An argillaceous sandstone sample with the
871 highest V/Al value, containing the most amount of chamosite and least amount of
872 glauconite (largely transformed into chamosite).

873

874 **Figure 8.** Micro-spot element analyses showing the compositional changes from

875 glauconite to chamosite. **(a)** Cross plot of K_2O vs. TFe_2O_3 , showing that the
876 transformation from glauconite to chamosite requires addition of Fe but loss of K. **(b)**
877 Cross plot of MgO vs. TFe_2O_3 , showing that the transformation from glauconite to
878 chamosite requires addition of Fe and Mg. **(c)** Cross plot of Al_2O_3 vs. TFe_2O_3 , showing
879 that the transformation from glauconite to chamosite requires addition of Fe and Al. **(d)**
880 Cross plot of SiO_2 vs. TFe_2O_3 , showing that the transformation from glauconite to
881 chamosite requires addition of Fe but loss of Si.

882

883 **Figure 9.** Mg/Fe vs. Al/Si ratios of chamosites from different geological settings
884 (modified from [Damyanov and Vassileva 2001](#)). Most of the chamosites from the
885 Xiamaling Formation fall into the category of marine origin.

886

887 **Figure 10.** BSE images and EDS analyses of the glauconite-chamosite transformation. **(a)**
888 A glauconite particle that has been partially transformed to chamosite (light
889 gray–chamosite; gray–glauconite; dark gray–quartz). **(b)** EDS spectrum of the point “X”
890 in [Fig. 10a](#) showing that glauconite is mainly composed of K, Fe, Mg, Al, Si, and O. **(c)**
891 EDS spectrum of the point “+” in [Fig. 10a](#), showing that chamosite is composed of
892 similar elements as those of glauconite, but with obviously high Fe and low K contents;
893 **(d)** A glauconite particle that has been transformed to chamosite with reticular texture
894 (light gray–chamosite; gray–glauconite; dark gray–quartz). **(e)** BSE image with high
895 magnification, showing partial replacement of glauconite (Gl) by chamosite (Ch) and the
896 retention of flakes across the mineral boundary (arrows). **(f)** BSE image with high
897 magnification, showing a glauconite particle that has largely been transformed into

898 chamosite (light gray), with several 100–800 nm thick glauconite strips (dark gray). (g) A
899 glauconite particle that has been completely transformed to chamosite (light gray) with
900 no glauconite relics but a quartz ring (dark gray). In all EDS analyses, Pt results from
901 coating.

902

903 **Figure 11.** Elemental mapping and EDS analyses of the glauconite-chamosite
904 transformation. (a) A BSE image, the same as [Fig. 10f](#), showing the selected area for
905 elemental mapping (white rectangular area). Arrows point to glauconite relics. (b–d)
906 Elemental mapping of Fe, K, and Si, respectively, showing that chamosite has higher Fe,
907 but low K and Si contents than glauconite. (e) EDS spectrum of the spot “X” in [Fig. 11a](#),
908 showing that glauconite is mainly composed of K, Fe, Mg, Al, Si, and O. (f) EDS
909 spectrum of spot “+” in [Fig. 11a](#), showing that chamosite is composed of similar elements,
910 but with obviously higher Fe and lower K contents than glauconite.

911

912 **Figure 12.** Cross plot of Fe_{HR}/Fe_T vs. Fe_P/Fe_{HR} , showing that all samples ($n = 10$) from
913 glauconite- and chamosite-bearing strata fall into ferruginous area.

914

915 **Figure 13.** Schematic diagram showing the mineral structural changes during
916 glauconite-chamosite transformation (modified from [Drits et al. 2001](#)). (a)
917 Transformation of glauconite to berthierine through the removal of interlayer cations and
918 one tetrahedral sheet of the 2:1 layer. The vacant octahedron is occupied by Mg^{2+} and
919 Fe^{2+} cations adsorbed from solution. (b) Transformation of glauconite to berthierine by
920 removal of interlayer cations accompanied by the inversion of upper tetrahedral sheets of

921 2:1 layers and the occupation of vacant octahedron by Mg^{2+} and Fe^{2+} cations adsorbed
922 from solution. (c) Transformation of berthierine layers into chamosite layers through
923 inversion of the tetrahedral sheets of the even 1:1 layers.

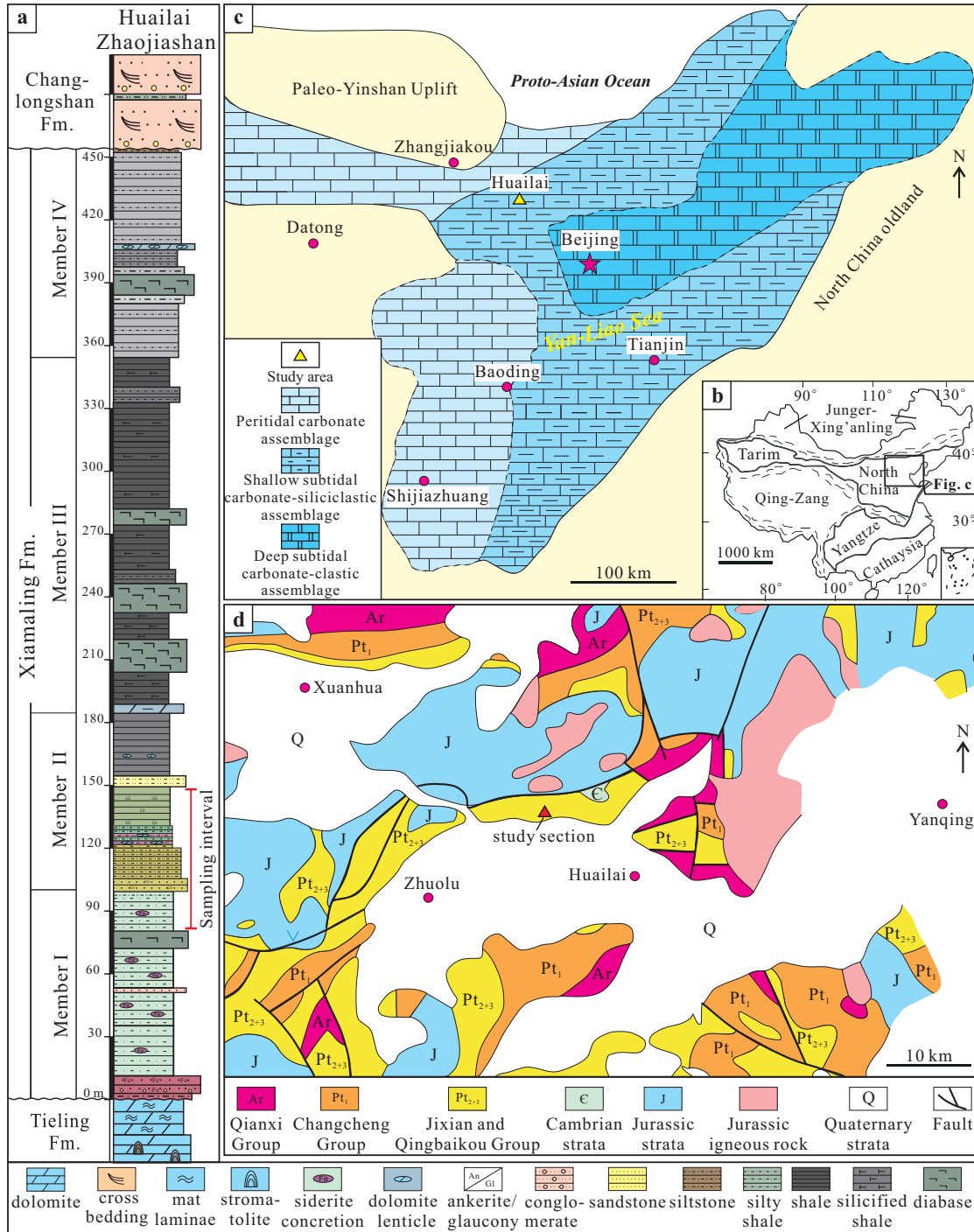


Figure 1

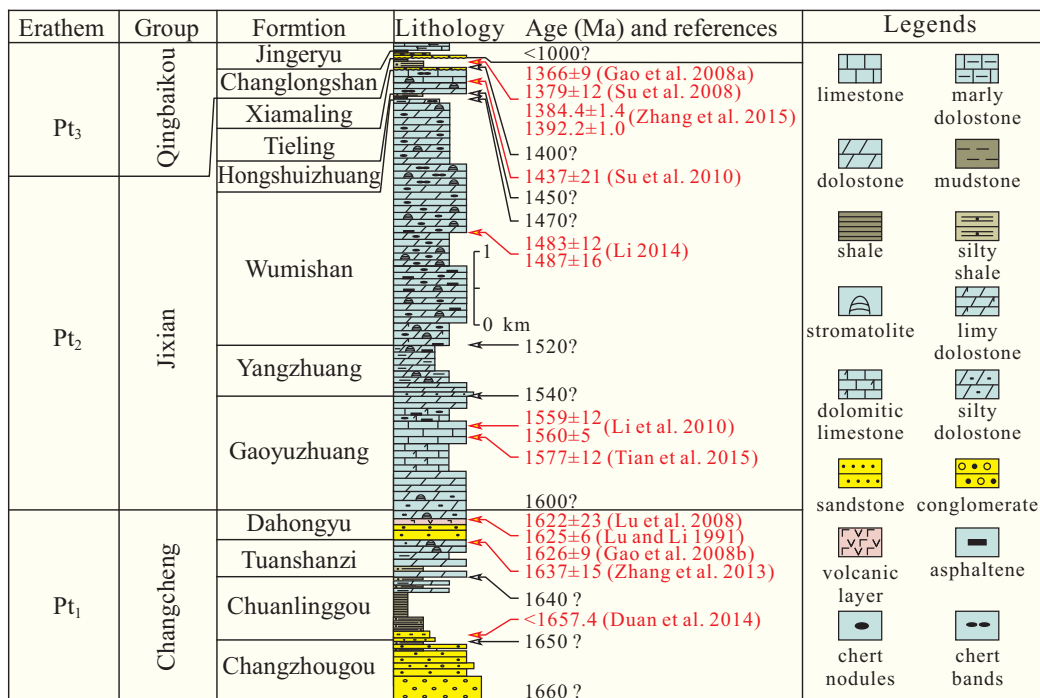


Figure 2

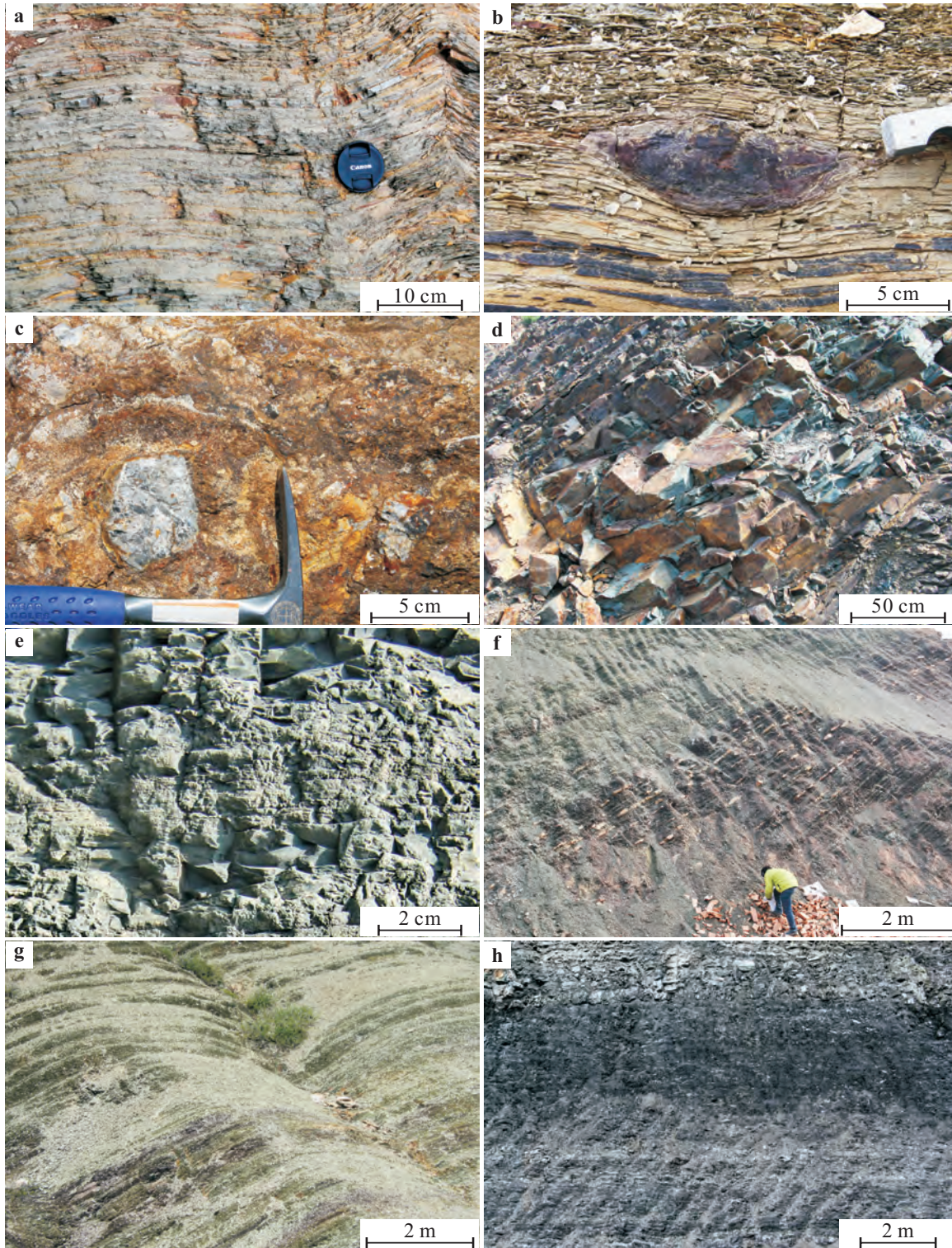


Figure 3

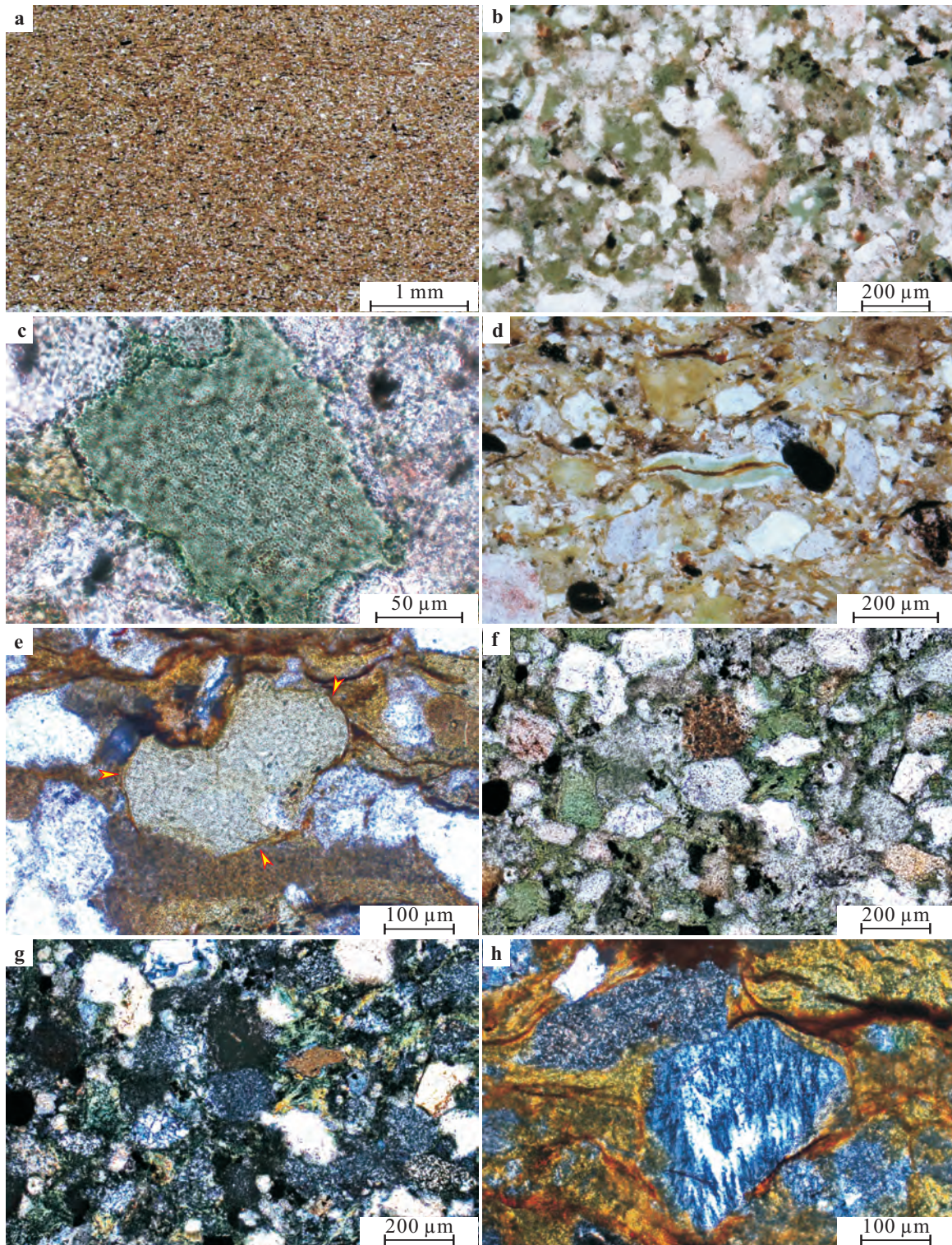


Figure 4

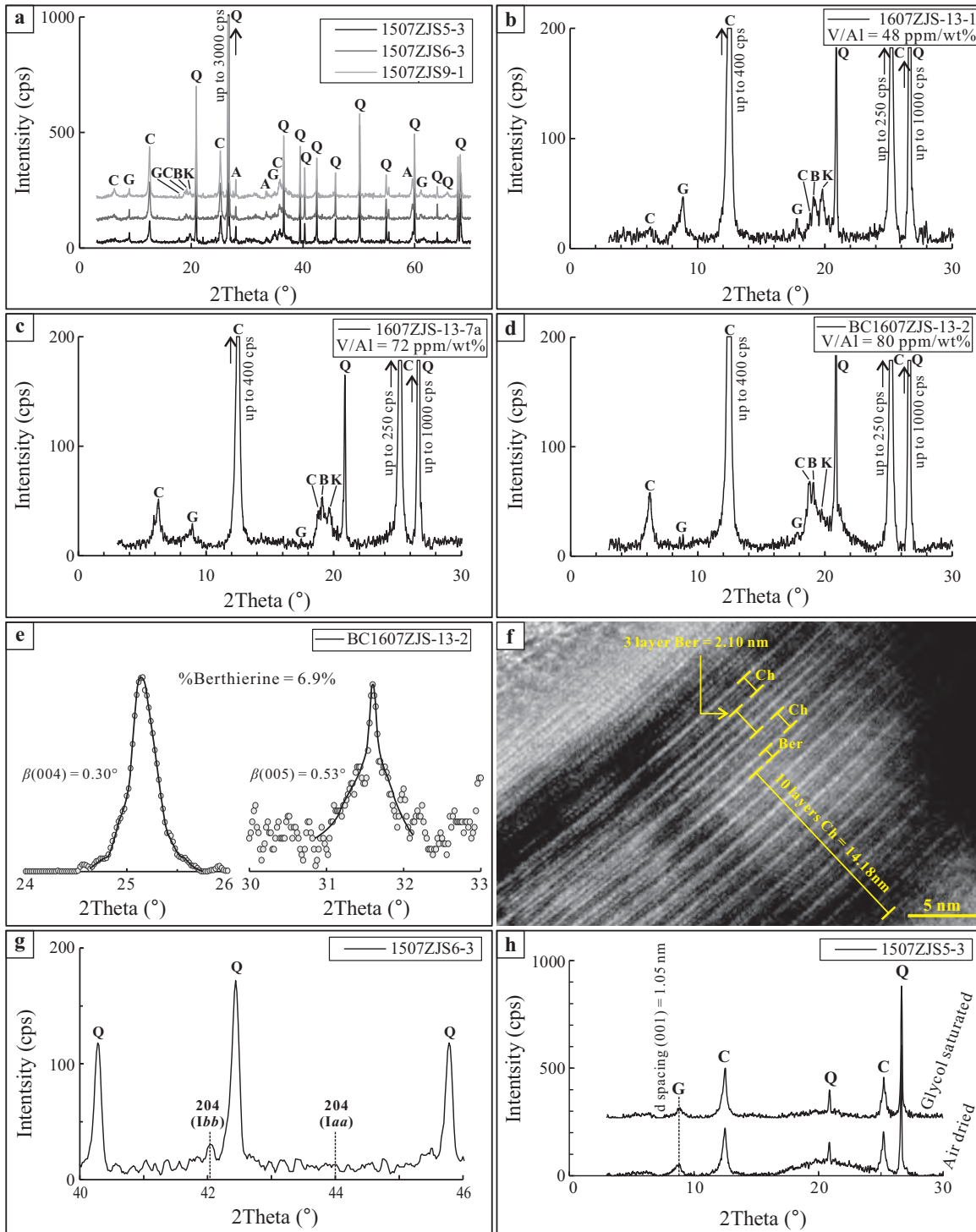


Figure 5

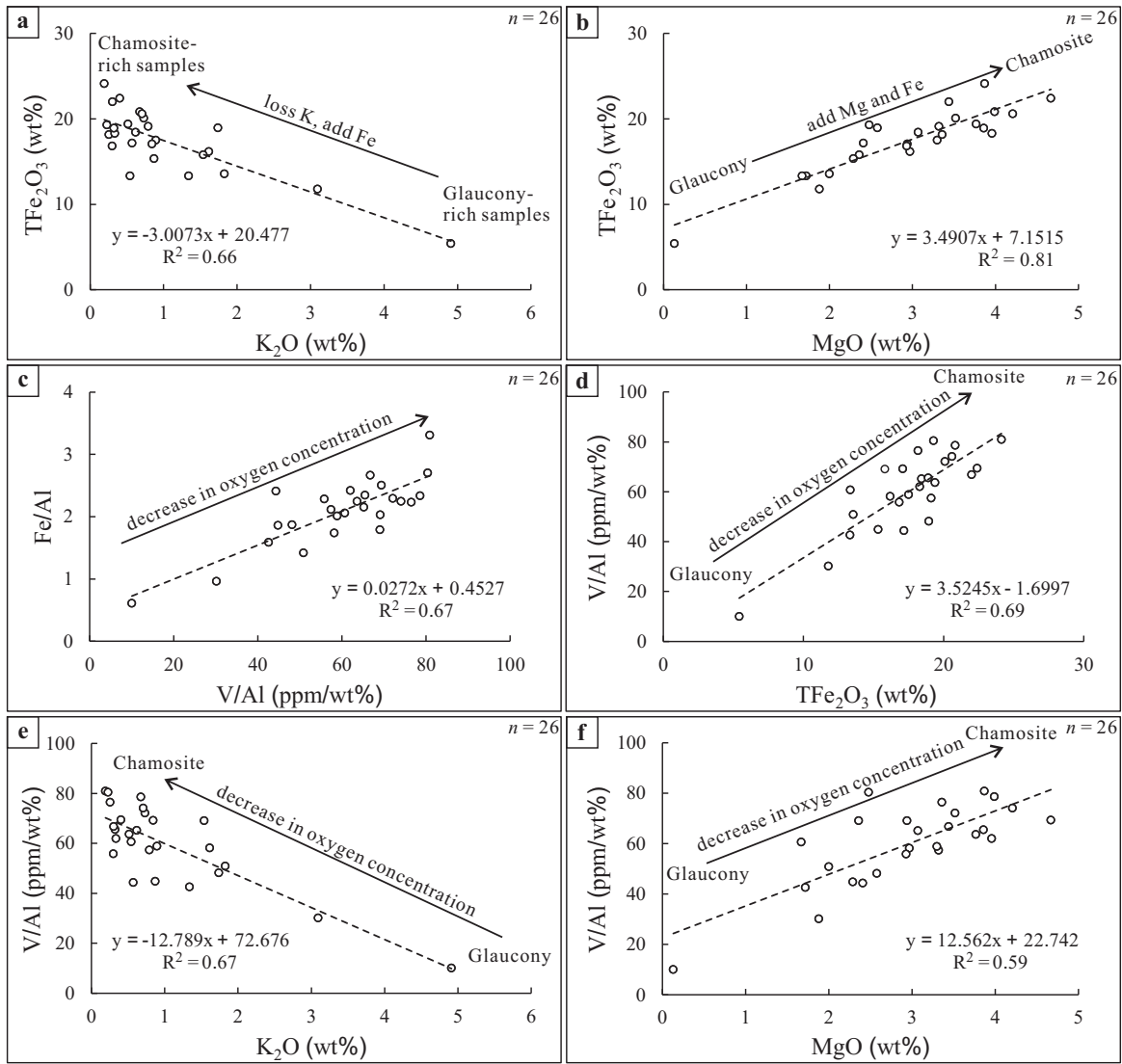


Figure 6

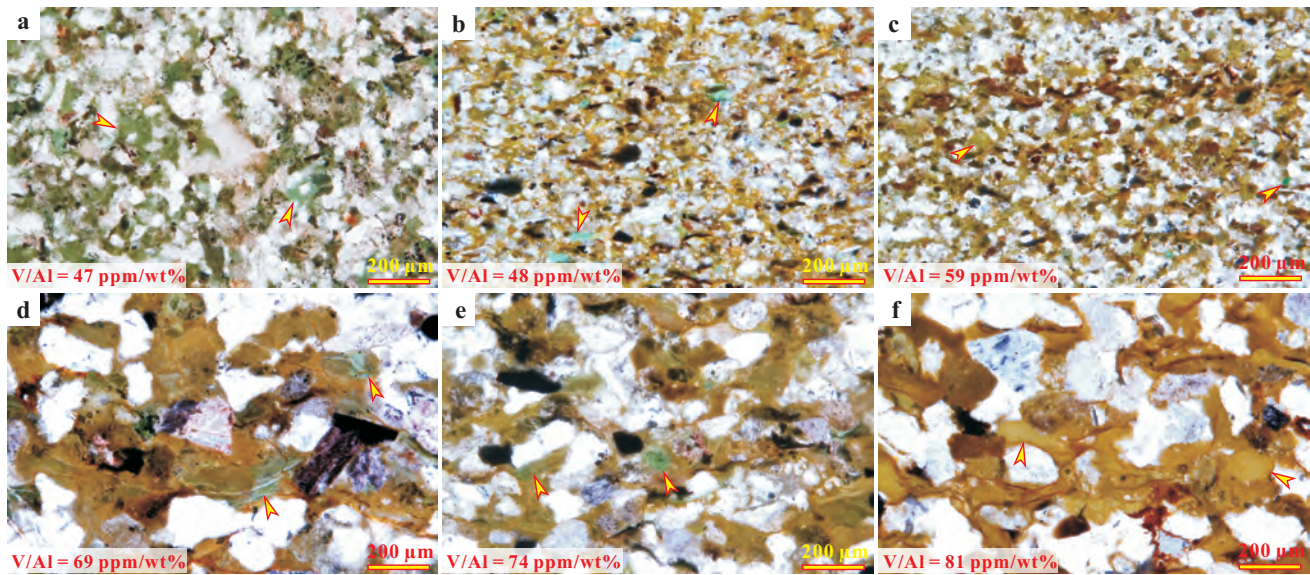


Figure 7

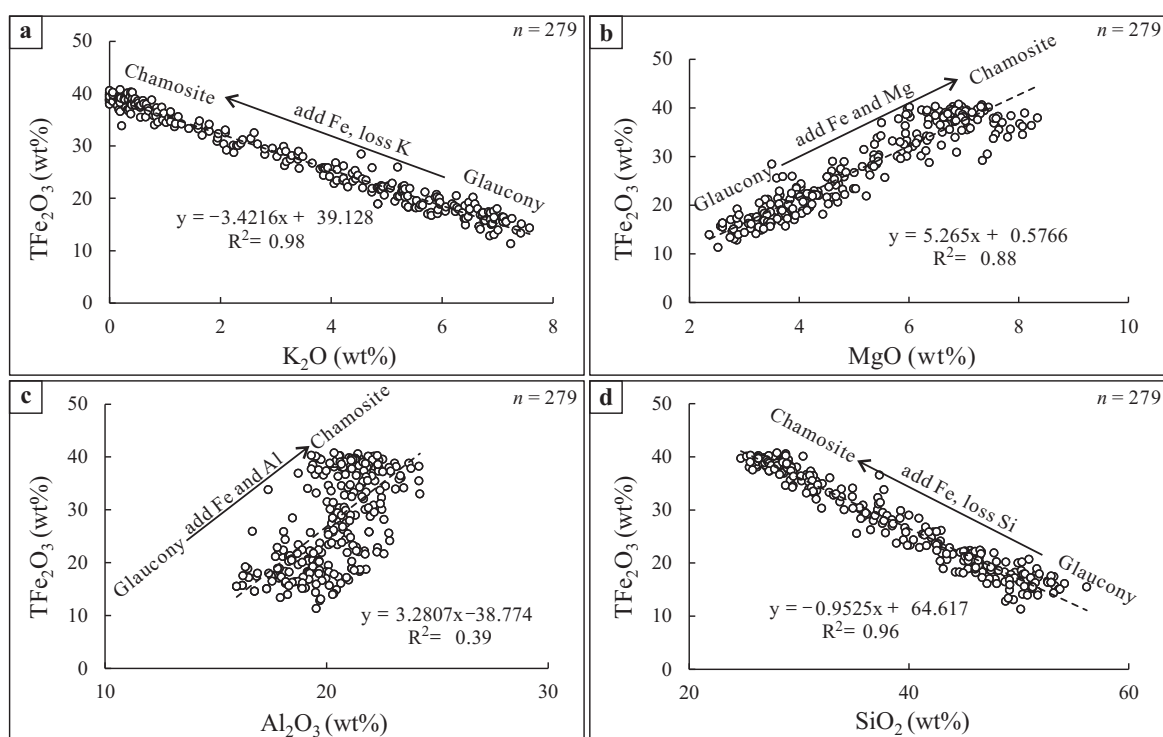


Figure 8

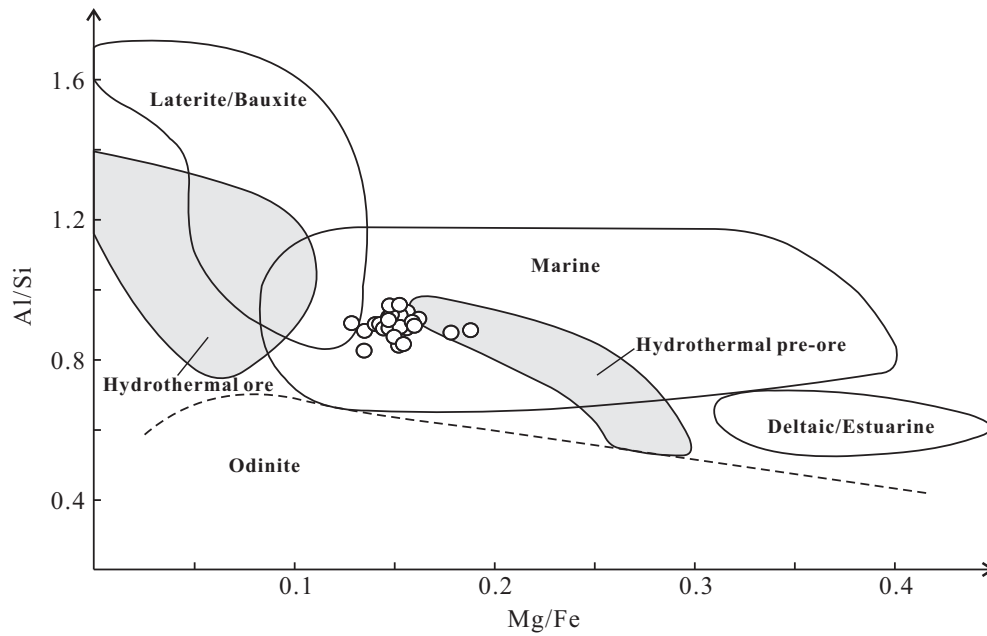


Figure 9

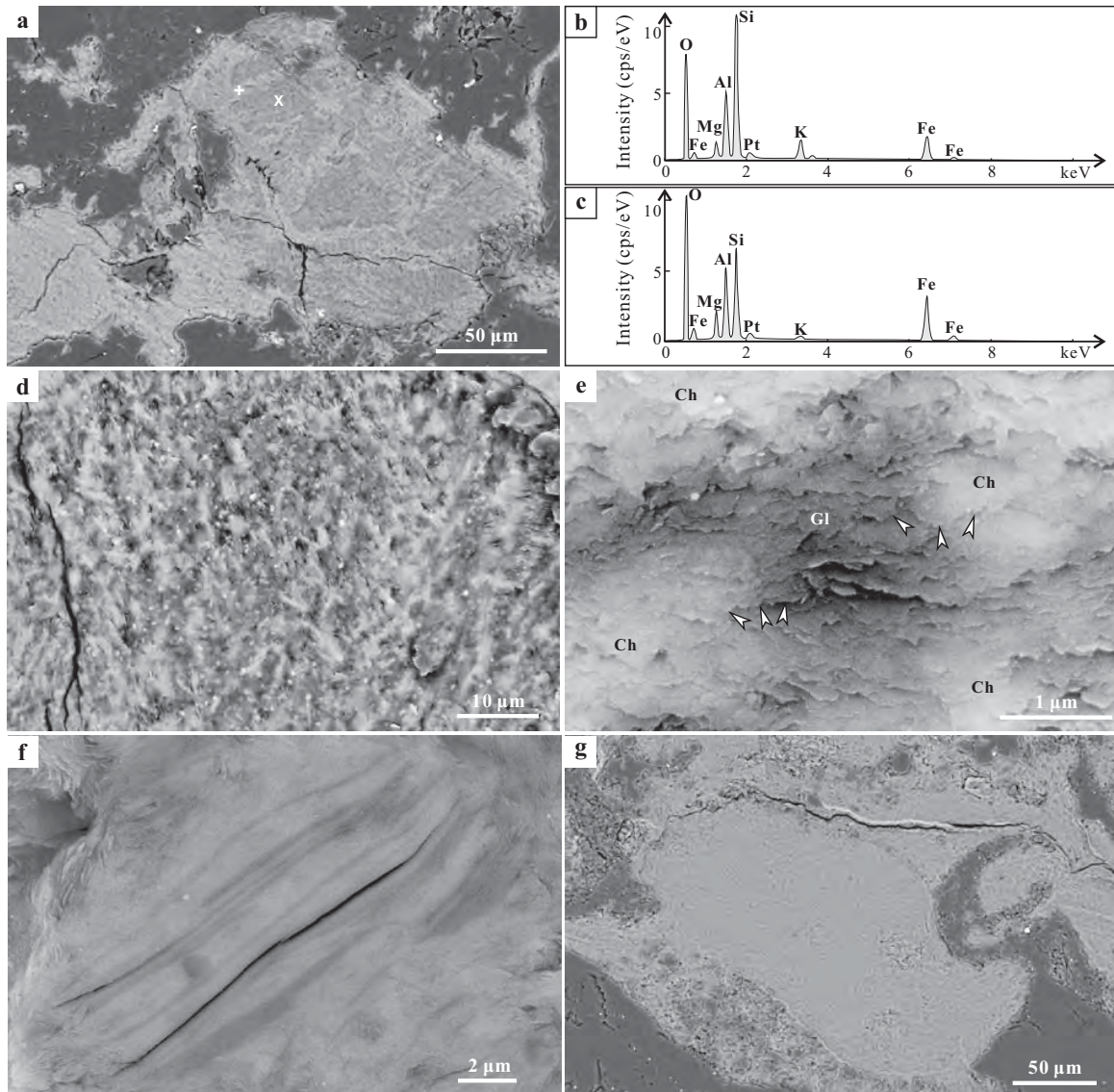


Figure 10

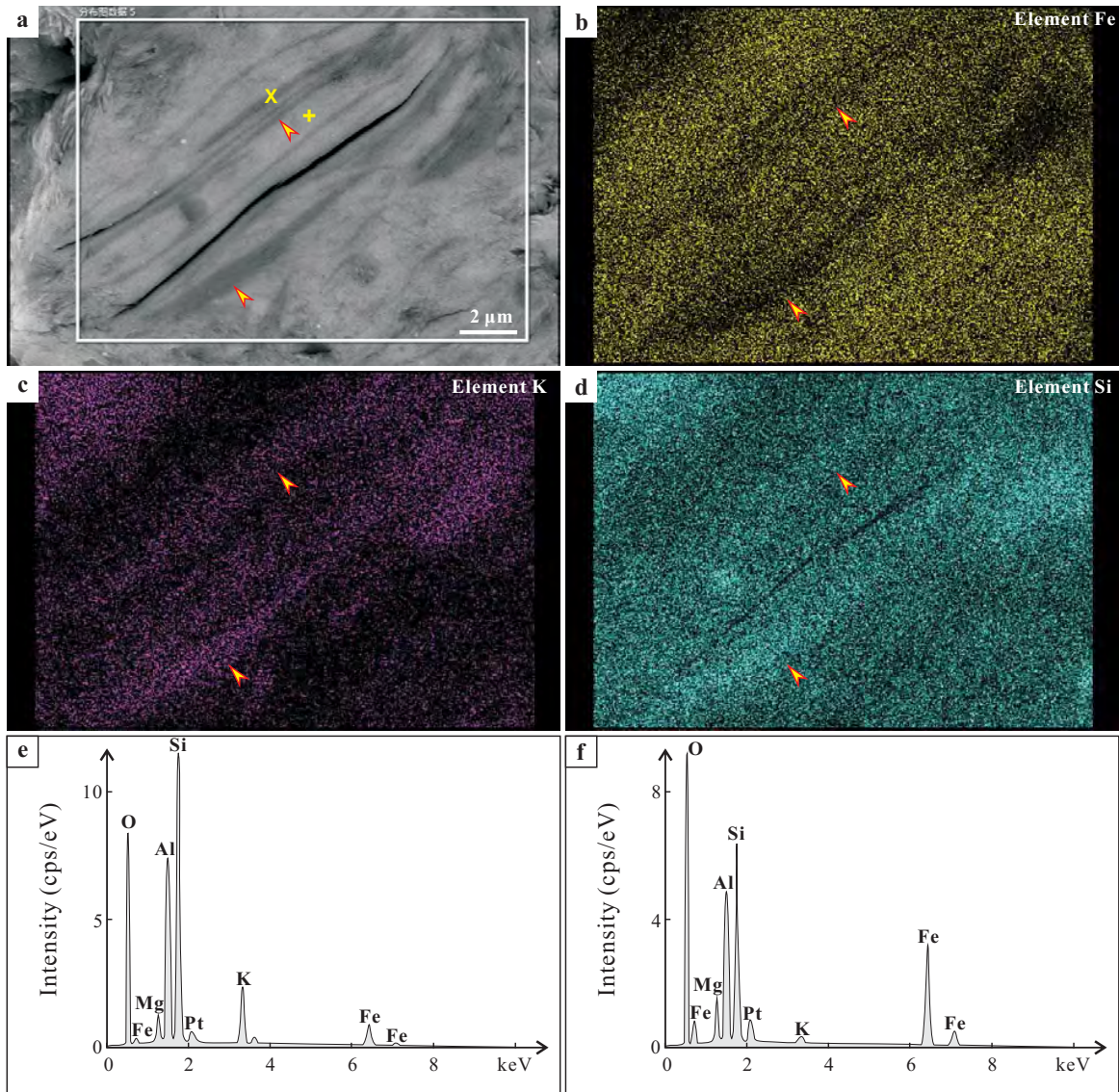


Figure 11

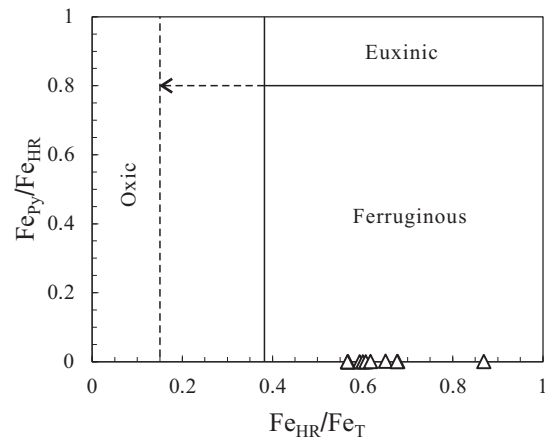


Figure 12

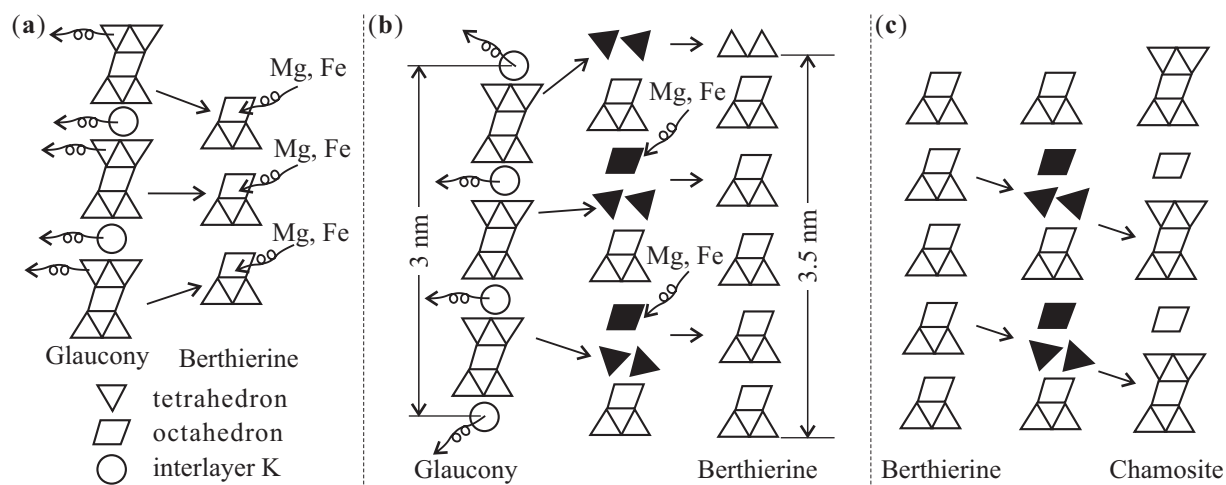


Figure 13